SEARCHING FOR SUBSTRUCTURE IN THE STELLAR POPULATIONS OF DWARF AND GIANT GALAXIES

Ryan A. Lambert

Submitted to the faculty of the University Graduate School
in partial fulfillment of the requirements
for the degree
Doctor of Philosophy
in the Department of Astronomy
Indiana University
December 2021

Accepted by the Graduate Faculty, Indiana University, in partial fulfillment of the requirements for the degree of Doctor of Philosophy.

Doctoral Committee

_____
Katherine Rhode, Ph.D.

_____
Enrico Vesperini, Ph.D.

_____
Samir Salim, Ph.D.

_____
Charles Horowitz, Ph.D.

December 15, 2021

To that pale thing that hides behind the moon, whispering eldritch secrets into my ear. May the prize ever be worth the price.

ACKNOWLEDGEMENTS:

None of this would have been possible without the help of so many people. Dr. Richard Gray, thank you for taking the slightly awkward first year undergrad under your wing. I have so many fond memories of working with you and Ian. The App State physics undergrads, Kyle, Jesse, Jess, Selby, Nathan, Tyler, there are too many to properly name. Our late nights in the Lindsey Room smashing our heads against the wall prepared me for this. I hope you're all doing well.

Thank you to my advisors, Kathy Rhode and Enrico Vesperini. It can't have been easy dual-advising but you gave me good advice and I will forever appreciate the support you've shown me these past 7 years. Your guidance has helped me grow as a scientist and a person. Thank you for your patience.

Thank you, my fellow IU graduate students. Jeff, Zack, and Amanda, our board game nights are something I miss. Hannah, I swear I will get back into rock climbing once this pandemic is done and I have you to thank for that. Playing super smash bros. at your place and all those sweet baked goods were a blast, Nick. Caug and Madison, you two have given me a level of love and support that I am frankly still flabbergasted by. Sam and Chris our first year really cemented our bond and know that no matter where life takes us, you can call on me. I never expected to meet so many wonderful people who would come to mean so much to me. I love you all.

Thank you Emory, Chris, and Eric. It's amazing to me that even states away for most of the year, you have kept me included in the group. Shane and Adam, I met you later, but I consider you part of this group as well. You're all some of my best friends

Thank you, Liz Culpepper. This past year has been both one of the toughest and one of the best years of my life. You kept me sane during a pandemic and laughing when I was frustrated. You were a light in the dark and I cannot wait to see where life takes us next. Mom, you raised me to be compassionate, curious, and to be stubborn to the point of stupidity. That last one helped the most, I think. Jason, Jess, and Blair, you all have been so kind to me throughout this process and your unfailing support is something I don't think I can ever truly repay. Thank

you so much.

Ryan A. Lambert

Searching for Substructure in the Stellar Populations of Dwarf and Giant Galaxies

In the paradigm of hierarchical galaxy evolution, substructure is expected to form through tidal interactions, accretion events, or mergers of galaxies and proto-galaxies. In this thesis I investigate the spatial distribution of Red Giant Branch (RGB) stars within three Andromeda dwarf satellite galaxies (Lacerta I, Cassiopeia III, and Perseus I) and the spatial distribution of globular clusters around two massive elliptical galaxies (M86 and M84) in an effort to identify such substructure.

In the process, I characterize the three Andromeda dwarf satellites by estimating their structural and positional parameters (ellipticity, position angle, half-light radius, Sersic index, Right Ascension and Declination of the galaxy centers). I find a chain of over-densities along the west side of Lacerta I and two filaments northwest and southeast of the center of Cassiopeia III that may be coherent substructures. I find no evidence of substructure within the RGB population of Perseus I, possibly due to its relatively isolated environment.

Within the globular cluster systems of M86 and M84, I find three features of interest. The peak surface density of the globular cluster system of M86 is offset from the galaxy's center, which may be at least partly due to the presence of the dwarf elliptical galaxy NGC 4406B. There exists a bridge of globular clusters between the M86 and M84 with a higher surface density than would be expected. Finally a boxy iso-density contour extends along the southeast side of the globular cluster system of M86.

Katherine Rhode, Ph.D.

Enrico Vesperini, Ph.D.

Samir Salim, Ph.D.

Charles Horowitz, Ph.D.

Table of Contents

List of Tables

List of Figures

Chapter 1

Introduction

1.1 Hierarchical Structure Formation and Galaxy Assembly

Within the current paradigm of Λ Cold Dark Matter (ΛCDM) cosmology, the galaxies seen today were formed hierarchically, through the continuous merging and accretion of smaller protogalactic fragments. In this hierarchical formation scenario, small fluctuations in the matter density distribution in the early universe began to collapse and accrete the surrounding matter, forming structures that grew over time. This process continued with more massive structures forming from these constant accretion events, eventually resulting in the galaxies we observe today. Evidence of these accretion and merging events would in many cases remain for timescales of a few billion years and be visible as streams, shells, and stellar over- and under-densities within and around galaxies of all sizes, as this is a process that happens across many different scales.

Simulations of hierarchical merging and matter accretion within the context of a ΛCDM Universe have been fairly successful at recreating the observed overall distribution of matter (e.g., Springel et al. 2005; Vogelsberger et al. 2014; Schaye et al. 2015) and producing galaxies with realistic properties that are generally well-matched to the properties observed today (e.g., Springel et al. 2008; Hopkins et al. 2014, 2018). In light of this, much of the recent work on this topic has focused on gathering obser-

[1]This chapter has paragraphs based on the paper Lambert, R.A., Rhode, K.L., & Vesperini, E. 2020, ApJ, 900, 45., "Substructure in the Globular Cluster Populations of the Virgo Cluster Elliptical Galaxies M84 and M86"

vational evidence for hierarchical growth through the identification of stellar streams and tidal interactions, which are thought to be the hallmark of low-mass galaxies having been accreted by more massive galaxies. The Sagittarius dwarf galaxy (Ibata et al. 1994) and the stellar streams associated with it (Belokurov et al. 2006) are some of the most well-studied examples of this type of hierarchical accretion in the Milky Way. Recent data from the Gaia mission (Gaia Collaboration et al. 2016) and other large-scale surveys, and analyses that combine kinematic data with information about chemical abundances and/or specific stellar populations, have led to discoveries of additional substructures in the Galaxy and brought renewed attention to this topic (e.g., Belokurov et al. 2018; Deason et al. 2018; Malhan et al. 2018; Myeong et al. 2018; Helmi et al. 2018; Shipp et al. 2018; Naidu et al. 2020; Li et al. 2021; Malhan et al. 2021; Martinez-Delgado et al. 2021).

The Andromeda galaxy (M31) has been studied in detail as well. Structures formed from spatial over-densities of the Red Giant Branch (RGB) population, e.g. the Giant Stellar Stream, have been found in the outer halo of M31 by using resolved RGB star maps (Ibata et al. 2001; Ferguson et al. 2002). Using the surface density of resolved RGB stars, it is possible to infer the surface brightness distribution of the underlying light; structures revealed by this technique, such as faint streams and clumps of RGB stars, suggest a rich history of accretion events and tidal interactions for M31.

1.2 Substructure in Resolved Stellar Populations of Nearby Dwarf Galaxies

As hierarchical formation is a process that occurs over many different scales, it can be expected that evidence of interactions would be visible not only in massive galaxies but dwarf galaxies as well. Dwarf galaxy-sized structures are predicted to be among the earliest structures to form in the universe and understanding their evolution is

fundamental to questions about galaxy formation and evolution. Within the Local Group, studies of dwarf galaxies are advantaged by their often large angular extents across the sky and resolvable RGB populations. Studying the spatial positions of the RGB populations, paired with kinematic and metallicity information when possible, could reveal the signatures of hierarchical galaxy formation processes.

Evidence of tidal interactions affecting the structure of dwarf galaxies has been growing. Some examples of this include Geha et al. (2005), where 2D spectroscopy was used to determine that NGC 770, a low-luminosity elliptical galaxy gravitationally bound to the massive spiral galaxy NGC 772, hosts a core rotating counter to the rest of the galaxy. Although it is possible that the core of NGC 772 formed via interactions, Geha et al. (2005) favor a formation scenario in which NGC 770 instead underwent a minor merger with a smaller dwarf galaxy.

Another example of evidence of dwarf tidal interactions was presented by Paudel et al. (2015) observed a tidal stellar filament connecting UGC 6741 and UGC 6741B. The 15 kpc filament appears as diffuse light with several star-forming regions appearing as clumps along the length of it. Additionally they obtained archival H I of UGC 6741 that also covered UGC 6741B and found the mass to blue light ratio was similar to what would be expected from a blue compact dwarf galaxy. This led Paudel et al. (2015) to suggest that UGC 6741 may be an example of the formation channel predicted by Meyer et al. (2014), where some early-type dwarf galaxies have a phase as a blue compact dwarf. This evolution would likely be a result of the interaction UGC 6741 is currently undergoing.

Evidence of a possible merger was found by Wang et al. (2019) when they studied the stellar population of the Fornax dwarf spheroidal galaxy. Using archival data from the Dark Energy Survey, they identified shell-like structures to the southwest and northeast of the galaxy center that may indicate the existence of a disrupted stellar system. They note this scenario is supported by chemical and kinematic studies of

Fornax which revealed complex dynamical features suggestive of one or more stellar systems with distinct angular momenta having merged with Fornax (Amorisco & Evans 2012; del Pino et al. 2017).

Around the dwarf spheroidal galaxy DDO 44, Carlin et al. (2019) discovered a tidal stream in the direction of NGC 2403, a Local Volume galaxy that likely hosts DDO 44. The stream was found through a density map of RGB candidate stars obtained from observations made with the Subaru telescope. The stream is estimated to be approximately 50 kpc in length and accounts for 20-30% of the total luminosity of the galaxy. In the paper, it is hypothesized that the ongoing disruption of DDO 44 has resulted in quenching of its star formation and an increase of star formation within NGC 2403.

While the previous studies mentioned have focused on evidence of interactions between dwarf galaxies and their nearby hosts or companions, the Solo Dwarf Galaxy survey (Higgs et al. 2021) observed 44 isolated ($>$ 300kpc from M31 or the Milky Way) dwarf galaxies less than 3 Mpc from the Milky Way. The intent of the survey was to provide a homogeneous analysis of these galaxies to minimize systematic errors in such a small statistical sample. In Higgs et al. (2021), they characterized a subset of 12 dwarf galaxies in the survey using integrated light profiles for the crowded, inner regions of each galaxy and radial profiles of the RGB stellar populations in the outer regions. With these profiles they determined structural parameters and created surface density maps of each dwarf galaxy in the subset. No substructure was found in the outer regions of the examined dwarfs, adding a useful constraint to the role environment plays in the evolution of dwarf galaxies.

1.3 Substructure Using Luminous Tracers around Distant Galaxies

Beyond the Local Group, deep observations of galaxies have revealed streams, shells, and satellites using resolved RGB stars as well as unresolved low surface brightness

(LSB) features (e.g., Janowiecki et al. 2010; Crnojevic et al. 2016; Mihos et al. 2017). However, in galaxies well beyond the Local Group, RGB stars are unresolved and a different tracer of hierarchical assembly processes and tidal interactions is required. At these distances, identifying substructure within dwarf galaxies is not as feasible and our focus shifts to tracers that correlate with substructure in massive galaxies. Globular clusters (GCs) have a number of properties that make them well-suited for this task.

GCs are compact stellar systems with typical masses ranging from $\sim 10^4$ $M_\odot$ to $\sim 10^6$ $M_\odot$. They are highly luminous objects and therefore visible up to distances of hundreds of Mpc (e.g., Blakeslee 1999; Mieske et al. 2004). They are ubiquitous across all galaxy types, with giant galaxies typically hosting hundreds or thousands of GCs (e.g., Rhode 2012; Young 2016). Furthermore, GC metallicities have been shown to contain information about hierarchical galaxy assembly processes. The Milky Way has two populations of GCs with different mean metallicities, and the abundances and other properties of these two populations have been used to probe the Galaxy's past history (Zinn 1985; Armandroff & Zinn 1988). Most other massive galaxies have GC systems that show multiple peaks in their color distributions (e.g., Brodie & Strader 2006, and references therein). For integrated colors of stellar populations older than $\sim 2-6$ Gyr, these color differences can indicate a difference in metallicity, with bluer colors corresponding to lower metallicities and redder colors corresponding to higher metallicities (e.g., Young 2016). The presence of multiple color peaks in the GC systems of some galaxies is commonly interpreted as evidence that such galaxies have undergone two or more major epochs of star formation, possibly triggered by mergers or accretion events (e.g., Ashman & Zepf 1992; Zepf & Ashman 1993; Li & Gnedin 2014; El-Badry et al. 2019). Moreover, the spatial distributions of the GC subpopulations have been shown to differ in many galaxies, with blue/metal-poor GCs typically covering a larger radial extent than their red/metal-rich counterparts

(e.g., Brodie & Strader 2006, and references therein). While this spatial difference may have multiple causes, one hypothesis is that a large proportion of the metal-poor GCs in massive galaxies were deposited through accretion events (Côté 1999; Forbes & Bridges 2010).

GCs have also been shown to trace substructure within and around galaxies. For example, Lim et al. (2017) performed a study of the GCs in the early-type "shell" galaxy NGC 474 and found a significant correlation between the shell and stream structures and the GC spatial positions. Furthermore, previous studies have reported similar results for the M31 GC system (see Mackey et al. 2010; Ferguson & Mackey 2016, and references therein), finding a strong correlation between the spatial position of GCs within the system and stellar streams.

Since not all galaxies have readily visible substructure to compare to GC positions, another approach is to identify deviations in the spatial positions of GCs from the expected symmetric distribution of an unperturbed GC system. Bonfini et al. (2012) found an azimuthal asymmetry along the northeast-southwest direction in the GC system of the elliptical galaxy NGC 4261. D'Abrusco et al. (2013) recovered this same feature in NGC 4261 using the K-Nearest Neighbors (KNN) algorithm to estimate the surface density at various points in the field. In doing so, D'Abrusco et al. (2013) probed for radial and azimuthal asymmetries within the NGC 4261 GC system and found that the over-density forms a broken shell or spiral-like pattern. D'Abrusco et al. (2015) probed the cores of the GC systems of the 10 brightest Virgo galaxies for anomalies and found substructures of varying complexity and sizes ($\sim 0.5''$ to several arcminutes in length) in all of the observed systems. When studying the Fornax galaxy cluster, D'Abrusco et al. (2016) found an over-density within the NGC 1399 GC system. This over-density is dominated by the blue GCs and stretches from east to west, connecting NGC 1399's GC system to the GC systems of neighboring galaxies. Furthermore, the over-density of blue GCs in Fornax has been shown to be

associated with a region of intracluster light within the core of the cluster (Iodice et al. 2017). Durrell et al. (2014) and Powalka et al. (2018) identified GC population features within M87 (NGC 4486) and in the larger Virgo Cluster environment using Kernel Density Estimation (KDE) surface density maps. Durrell et al. (2014) found the spatial extent of the metal-poor GC populations extends much farther ($\sim$400 kpc from the galaxies) than metal-rich populations around M87 and M84 (NGC 4374), implying that intracluster GC populations are primarily comprised of metal-poor GCs. Dividing their sample into three age bins, Powalka et al. (2018) detected a spatial over-density of young GCs to the south of M87 that is not present in the intermediate age and oldest GC populations. This over-density was detected at the 5σ level and no host galaxy was detected within the over-density region. Madrid et al. (2018) created a surface density map of the Coma Cluster that highlighted evidence of several ongoing galaxy interactions. Such studies make it clear that GCs can be useful for discovering substructure in galaxy halos and exploring the history and evolution of galaxies and their stellar populations.

1.4 Organization of this Thesis

This thesis presents the results of a search for evidence of accretion and the presence of substructure in two different types of galaxies and two different settings: within the stellar populations of three nearby dwarf satellite galaxies in the Local Group, and in the globular star cluster populations of two massive Virgo Cluster galaxies. The organization of the thesis is as follows. Chapter 2 describes the various techniques that were tested and our final method for detecting substructure around the dwarf galaxies and the massive elliptical galaxies. Chapter 3 describes our data and the steps carried out to produce a list of positions and photometric measurements of the RGB populations of three Andromeda satellite dwarf galaxies along with the results of our applied methods for detecting substructure. Chapter 4 describes our data and the

steps carried out to produce a list of GC candidates in the field of M86 and M84. The chapter details substructure found in the field, including variations between the red and blue GC populations and kinematical analysis of GCs within the field. Chapter 5 presents of a summary of our results as well as a discussion of several possible avenues for future work in this area of research.

References

Amorisco, N. C. & Evans, N. W. 2012, ApJ, 756, L2.

Armandroff, T.E. & Zinn, R. 1988, AJ, 96, 92

Ashman, K.M. & Zepf, S.E. 1992, ApJ, 384, 50

Belokurov, V., Zucker, D. B., Evans, N. W., et al. 2006, ApJ, 642, L137

Belokurov, V., Erkal, D., Evans, N. W., et al. 2018, MNRAS, 478, 611

Bekki, K., & Yahagi, H. 2006, MNRAS, 372, 1019

Bekki, K., & Yahagi, H. 2009, Globular Clusters - Guides to Galaxies, 373

Blakeslee, J. P. 1999, AJ, 118, 1506

Bonfini, P., Zezas, A., Birkinshaw, M., et al. 2012, MNRAS, 421, 2872

Brodie, J.P. & Strader, J. 2006, ARA&A, 44, 193

Carlin, J. L., Garling, C. T., Peter, A. H. G., et al. 2019, ApJ, 886, 109.

Côté, P. 1999, AJ, 118, 406

Crnojevic, D., Sand, D.J., Spekkens, K., Caldwell, N., Guhathakurta, P., McLeod, B., Seth, A., Simon, J.D., Strader, J., & Toloba, E. 2016, ApJ, 823, 19

D'Abrusco, R., Fabbiano, G., Strader, J., et al. 2013, ApJ, 773, 87

D'Abrusco, R., Fabbiano, G., & Zezas, A., 2015, ApJ, 805, 26

D'Abrusco, R., Cantiello, M., Paolillo, M., et al. 2016, ApJ, 819, L31

Deason, A. J., Belokurov, V., Koposov, S. E., et al. 2018, ApJ, 862, L1

del Pino, A., Aparicio, A., Hidalgo, S. L., et al. 2017, MNRAS, 465, 3708. doi:10.1093/mnras/stw3016

Durrell, P. R., Côté, P., Peng, E. W., et al. 2014, ApJ, 794, 103

El-Badry, K., Quataert, E., Weisz, D. R., et al. 2019, MNRAS, 482, 4528

Ferguson, A. M. N., Irwin, M. J., Ibata, R. A., et al. 2002, AJ, 124, 1452

Ferguson, A. M. N., & Mackey, A. D. 2016, Tidal Streams in the Local Group and Beyond, 191

Forbes, D. A., & Bridges, T. 2010, MNRAS, 404, 1203

Forte, J.C., Martinez, R.E., & Muzzio, J.C. 1982, AJ, 87, 1465

Gaia Collaboration, Prusti, T., de Bruijne, J. H. J., et al. 2016, A&A, 595, A1

Geha, M., Guhathakurta, P., & van der Marel, R. P. 2005, AJ, 129,

Helmi, A., Babusiaux, C., Koppelman, H. H., et al. 2018, Nature, 563, 85

Higgs, C. R., McConnachie, A. W., Annau, N., et al. 2021, MNRAS, 503, 176.

Hopkins, P. F., Kereš, D., Oñorbe, J., et al. 2014, MNRAS, 445, 581

Hopkins, P. F., Wetzel, A., Kereš, D., et al. 2018, MNRAS, 480, 800

Ibata, R. A., Gilmore, G., & Irwin, M. J. 1994, Nature, 370, 194

Ibata, R., Irwin, M., Lewis, G., et al. 2001, Nature, 412, 49

Iodice, E., Spavone, M., Cantiello, M., et al. 2017, ApJ, 851, 75

Janowiecki, S., Mihos, J. C., Harding, P., et al. 2010, ApJ, 715, 972

Lambert, R. A., Rhode, K. L., & Vesperini, E. 2020, ApJ, 900, 45.

Li, H., & Gnedin, O. Y. 2014, ApJ, 796, 10

Li, T. S., Ji, A. P., Pace, A. B., et al. 2021, arXiv:2110.06950

Lim, S., Peng, E. W., Duc, P.-A., et al. 2017, ApJ, 835, 123

Mackey, A. D., Huxor, A. P., Ferguson, A. M. N., et al. 2010, ApJ, 717, L11

Madrid, J. P., O'Neill, C. R., Gagliano, A. T., et al. 2018, ApJ, 867, 144

Malhan, K., Ibata, R. A., & Martin, N. F. 2018, MNRAS, 481, 3442.

Malhan, K., Yuan, Z., Ibata, R. A., et al. 2021, ApJ, 920, 51.

Martinez-Delgado, D., Cooper, A. P., Roman, J., et al. 2021, arXiv:2104.06071

Meyer, H. T., Lisker, T., Janz, J., et al. 2014, A&A, 562, A49.

Mieske, S., Infante, L., Benítez, N., et al. 2004, AJ, 128, 1529

Mihos, J. C., Harding, P., Feldmeier, J. J., et al. 2017, ApJ, 834, 16

Muzzio, J.C., Martinez, R.E., & Rabolli, M. 1984, ApJ, 285, 7

Myeong, G. C., Evans, N. W., Belokurov, V., et al. 2018, ApJ, 863, L28

Naidu, R. P., Conroy, C., Bonaca, A., et al. 2020, ApJ, 901, 48.

Paudel, S., Duc, P. A., & Ree, C. H. 2015, AJ, 149, 114.

Powalka, M., Puzia, T. H., Lançon, A., et al. 2018, ApJ, 856, 84

Ramos, F., Coenda, V., Muriel, H., et al. 2015, ApJ, 806, 242

Ramos-Almendares, F., Abadi, M., Muriel, H., et al. 2018, ApJ, 853, 91

Ramos-Almendares, F., Sales, L. V., Abadi, M. G., et al. 2020, MNRAS, 493, 5357.

Rhode, K. L. 2012, AJ, 144, 154

Schaye, J., Crain, R. A., Bower, R. G., et al. 2015, MNRAS, 446, 521

Shipp, N., Drlica-Wagner, A., Balbinot, E., et al. 2018, ApJ, 862, 114.

Springel, V., White, S. D. M., Jenkins, A., et al. 2005, Nature, 435, 629

Springel, V., Wang, J., Vogelsberger, M., et al. 2008, MNRAS, 391, 1685

Vogelsberger, M., Genel, S., Springel, V., et al. 2014, MNRAS, 444, 1518

Wang, M. Y., de Boer, T., Pieres, A., et al. 2019, ApJ, 881, 118.

Yahagi, H., & Bekki, K. 2005, MNRAS, 364, L86

Young, M.D., 2016, ProQuest Dissertations Publishing

Zepf, S.E., & Ashman, K.M. 1993, MNRAS, 264, 611

Zinn, R. 1985, ApJ, 293, 424

Chapter 2

Methods for Detecting Substructure in Stellar Systems

As explained in the Introduction, our goal was to use robust statistical techniques to search for evidence of substructures and tidal features in collections of stars and star clusters. This chapter describes the techniques we used and their various advantages and drawbacks. The approach used to detect substructure within the stellar systems of dwarf galaxies and globular cluster systems of massive elliptical galaxies involved creating a model of the distribution of resolved stars or star clusters and comparing the model predictions of the surface density at a given area to the observed data. The basic idea is to assume that the model of the stellar system represents an idealized distribution, and therefore any deviations from this idealized model are possible evidence that past tidal events have perturbed the stellar populations or deposited new stars/star clusters into the system.

2.1 Maximum Likelihood Estimation and Deriving a Likelihood Function

To accurately model our distributions we utilized a technique referred to as Maximum Likelihood Estimation (MLE). As described in Martin et al. (2008), this technique assumes the observable data are drawn from a model distribution of the user's choosing. A likelihood function is constructed from the model distribution and is used to quantify how well the structural parameters of the model fit the observed stellar distribution. For our distributions of resolved stars, our model is a Sersic profile because

they are flexible and yield reasonable fits. With this model, the parameters to estimate are the half-light radius (r_h), Sersic index (n), ellipticity (ϵ), position angle (θ), and the offset of the central galaxy coordinates from the NASA/IPAC Extragalactic Database (NED)[2] (ΔRA and ΔDec for right ascension and declination respectively). The background surface density– i.e., the surface density of foreground Galactic stars and unresolved background galaxies not associated with the stellar system – is another parameter in the model that can be estimated with MLE. However, we decide to use our own background surface density estimates of the fields in order to lower the number of free parameters the MLE is required to find.

The following derivation of the likelihood function of a Sersic profile is largely a combination of the work of Graham & Driver (2005) and Martin et al. (2008) rewritten here for ease of reference. Before we begin, though, it is necessary to define our measurement of radius, the elliptical radius. The elliptical radius is the length of the semi-major axis of an ellipse passing through a point in space, (X_i,Y_i). The elliptical radius can be expressed as

$$r_i = \left\{ \left[\frac{1}{1-\epsilon} (X_i cos\theta - Y_i sin\theta) \right]^2 + (X_i \sin\theta + Y_i cos\theta)^2 \right\}^{1/2} \tag{2.1}$$

where ϵ is the ellipticity of the stellar system and θ is the position angle measuring from north to east. X_i and Y_i are the distances from the centroid of the system in standard coordinates.

With the elliptical radius, r_i, defined, we begin the construction of our likelihood function by starting with our model, the Sersic function, expressed in terms of surface density:

$$\Sigma(r_i) = \Sigma_h \exp\left(-b_n \left(\left[\frac{r_i}{r_h} \right]^{\frac{1}{n}} - 1 \right) \right) \tag{2.2}$$

[2]The NASA/IPAC Extragalactic Database (NED) is funded by the National Aeronautics and Space Administration and operated by the California Institute of Technology.

Here $\Sigma(r_i)$ is the surface density at a given elliptical radius; Σ_h is the surface density at the half-light radius, r_h; n is the Sersic index describing how steeply the profile falls to zero; b_n is a constant that can be approximated as $b_n = 1.9992n - 0.3271$ (Prugniel & Simien 1997). This equation is also presented in Martin et al. (2008) (Equation 4).

The value of Σ_h is unknown but can be defined in terms of variables and constants that are known. Integrating Equation 2.2 over an area $A = \pi r^2(1-\epsilon)$ we find the number of objects within a given radius, $N(< r)$:

$$N(< r) = (1-\epsilon)\int_0^r \Sigma(r')2\pi r' dr' \tag{2.3}$$

When solved, Equation 2.3 becomes

$$N(< r) = \Sigma_h r_h^2 2\pi n(1-\epsilon)\frac{e^{b_n}}{(b_n)^{2n}}\gamma(2n,x) \tag{2.4}$$

where $x = b_n(\mathrm{r}/\mathrm{r}_h)^{1/n}$ (Equation 2 from Graham & Driver (2005) applied to an elliptical system) and $\gamma(2n,x)$ is the incomplete gamma function defined as

$$\gamma(2n,x) = \int_0^x t^{2n-1}e^{-t}dt \tag{2.5}$$

Solving Equation 2.4 for Σ_h and substituting the result into Equation 2.2 returns

$$\Sigma(r_i) = \left\{\frac{N b_n^{2n}\gamma(2n, b_n(r_{max}/r_h)^{1/n})}{r_h^2 2\pi n(1-\epsilon)}\right\}\exp\left(-b_n\left(\left[\frac{r_i}{r_h}\right]\frac{1}{n} - 1\right)\right) \tag{2.6}$$

where r_{max} is the furthest distance to which our data extends. This likelihood equation is complicated further by the addition of objects that do not belong to the stellar system within the data. We assume some constant background surface density Σ_b

throughout the field. The value of N, the number of objects associated with the stellar system, can likewise be rewritten in terms of this background surface density value, the area of the field, A, and the total number of objects in the sample, N_T, so that our final likelihood function is

$$\Sigma(r_i) = \left\{ \frac{(N_T - A\Sigma_b) b_n^{2n} \gamma(2n, b_n(r_{max}/r_h)^{1/n})}{r_h^2 2\pi n(1-\epsilon)} \right\} \exp\left(-b_n \left(\left[\frac{r_i}{r_h} \right]^{\frac{1}{n}} - 1 \right) \right) + \Sigma_b \tag{2.7}$$

Though the likelihood function presented in Equation 2.7 is complex, it has been constructed so as to account for all known variables that could explain the spatial distribution of objects in our data. In the next section we discuss our method for maneuvering through the parameter space defined by this function in an efficient and effective manner.

2.2 Probing the Parameter Space

Since maximizing the likelihood function requires probing the parameter space, MLE efficiency and accuracy are largely determined by the technique used to pick the next set of parameter values to attempt. In the case of a low dimensional parameter-space, creating an N-dimensional grid can be efficient and accurate but only if the grid resolution has been fine-tuned for the specific problem. While it is feasible to employ a grid search method due to the relatively few parameters that need to be estimated within our likelihood function, there are software packages available that can produce the same results more quickly.

The software we chose to utilize to probe the parameter space was the emcee package in Python, a Markov chain Monte Carlo (MCMC) Ensemble sampler. A more detailed explanation of the sampling algorithm is provided in Foreman-Mackey et al. (2013), but in short, the emcee python package utilizes a user-defined number of

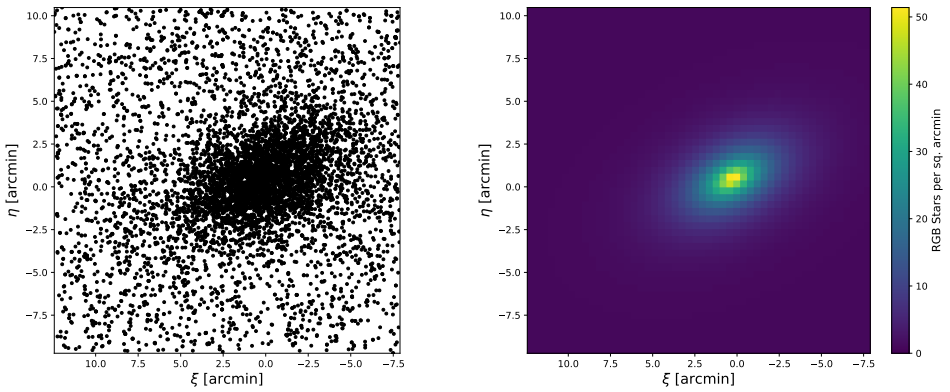

Figure 2.1 **Left:** The spatial distribution of the RGB stellar population of the dwarf galaxy Lacerta I. Positions are in standard coordinates with respect to the galaxy center. **Right:** The estimated surface density of the imaged Lacerta I RGB stellar population. The surface density of the population was estimated using the best-fitting structural parameters determined by MLE.

"walkers" with each returning the likelihood function result for different points in the parameter space. For a given walker, a new position in N-dimensional parameter space is proposed based on the position of every other walker. The acceptance probability is calculated for this new position and a random number between 0 and 1 is generated. If the acceptance probability equals or exceeds the randomly generated number, the position of the walker is updated. If the acceptance probability is less than the generated number, the proposed movement is discarded and the walker's position is left unchanged. Through this iterative process the underlying probability distribution of the N-dimensional parameter space can be mapped and the parameter values with the greatest likelihood can be determined for a given stellar distribution. An example of the predictive capability of the model can be seen in Figure 2.1. The left panel of Figure 2.1 is a plot of the Lacerta I dwarf galaxy RGB stellar population and the right panel is the estimated surface density at each grid cell using the best-fitting structural parameters determined with MLE. It can be seen that the model maintains a similar basic shape, position angle, and size as Lacerta I has in the left panel.

2.3 Residuals of the Inner and Outer Regions

With the best fitting parameters for our model determined, we can begin our search for substructure within the stellar system. Our method first examines the denser, inner region of the system. The inner region here is defined as everything within two half-light radii of the stellar system's center. This area is first broken into a grid and the expected stellar surface density is estimated at the center of each grid cell using our model. The stellar data can then be binned using the same grid and a surface density estimate can be obtained for each grid cell. Residuals are then calculated by subtracting the expected surface densities predicted by the model with the estimated surface density of the stellar data. The uncertainties produced by this method are Poissonian in nature because the numbers of objects in each bin are being counted.

The outer regions of the stellar system are characterized by a flattening of the surface density curve, as the background surface density dominates over the surface density of the stellar system. Since the data are sparser in this background-dominated region we search for substructure within it separately from the denser, inner region of the stellar system. To begin, we obtain several rough estimates of the background surface density by binning regions in our data set that are expected to fall entirely outside of the stellar system. A better estimate is calculated from the mean of these individual measurements.

The outer regions of the stellar system are too sparse to rely on histogram binning with a grid resolution comparable to the resolution used for the inner regions. Instead, we smooth the galaxy data using Kernel Density Estimation (KDE), a statistical technique that works by changing the probability density function of each object from a delta function to a pre-defined shape or "kernel" (Silverman 1986). We divide the field into a 100 by 100 grid and estimate the surface density of the smoothed data at the center of each grid cell. However, the smoothed surface density estimates

are no longer comparable to the unsmoothed background surface density. This issue is circumvented by generating the number of contaminating objects predicted by the background surface density and spreading them randomly across the field. Smoothing these randomly generated objects with KDE renders the now-smoothed background surface density comparable to our smoothed stellar system surface densities. Subtracting the smoothed background surface density from the smoothed surface density estimate of our data, we obtain residuals for the background. To determine the significance of any background structures, we compare the residuals to the standard deviation of the smoothed background surface density made from randomly generated objects and spread across the field. We avoid classifying the stellar system itself as an over-density by using the same prescription adopted in other studies (e.g., Kuzma 2017) where any over-densities greater than 4σ are considered part of the stellar system and excluded from further analysis.

2.4 Identifying Substructure within the M86 and M84 Globular Cluster Systems

Unfortunately, applying the method described in the previous section (Section 2.3) to the massive elliptical galaxies M86 and M84 is not feasible for several reasons. For one, the two galaxies are only a small projected angular distance apart, $\sim 16'$ ($\sim$85 kpc assuming the Virgo Cluster is 17 Mpc away), so their globular cluster systems are intermixed or at least projected onto one another in our image. Any likelihood function used must describe both globular cluster systems within the field even with the two systems interfering with the other; this problem may be worked around by the addition of a second Sersic function with its own set of structural parameters. However, the imaging of M84 is incomplete; Only half of the galaxy is within the field of view, as M86 was the primary target for the observations used. Defining a likelihood function that accounts for the half of the globular cluster system of M84 that

falls outside the image is a complex task and failure would not necessarily be easily identifiable from the results. For these reasons we do not attempt predictive modeling to find substructure within the M86/M84 field. Instead our method involves building density maps and finding features that cannot simply be described as fluctuations in the data and/or the projected overlap of the two systems.

Discarding our method for determining significance of substructure found in this region means a renewed effort must be made so that our technique for estimating the surface density of the globular cluster systems introduces as little bias as possible. As such we reviewed three techniques for estimating surface density to be certain our method would introduce the smallest bias possible: coarse binning, Kth-Nearest-Neighbor, and Kernel Density Estimation.

2.4.1 Binning

The simplest approach for characterizing the surface density variations across the field is to bin the data and then compare the surface density values in each bin. We split the field into a Cartesian grid and the surface density of each grid cell is equal to the number of objects in the grid cell divided by the area of the grid cell. This method falls short, however, when data sets have regions with widely varying surface densities. If a grid cell size is chosen that properly resolves the high density areas of the field, the cells will be too small to properly estimate the sparse, background regions. Likewise, if larger grid cells are used to properly resolve the sparsely populated background within the field, the high-surface density regions of the globular cluster system will be too poorly resolved to clearly reveal substructure.

2.4.2 Kth-Nearest-Neighbor

The Kth-Nearest-Neighbor (hereafter KNN) algorithm estimates the density at a point in space by finding the K nearest objects, where K is decided on by the user,

and calculating the area enclosing all K objects. This algorithm is able to quickly estimate the local density at any point in the field. In many ways, KNN is the inverse of binning. Rather than keeping a constant bin size with a variable number of objects in each bin, the KNN algorithm has a fixed number of objects but a variable amount of area within which those objects may be found. This has the added benefit of always returning a surface density estimate that is greater than 0. The algorithm has previously seen use in substructure detection research (D'Abrusco et al. 2013, 2015, 2016) and is quite flexible, with the choice of K value emphasizing substructure of different scales.

However, we found that over-densities in the sparsely populated background would be inflated far beyond the objects creating the over-density. Since the background is so sparse we found that the same few objects could be the closest neighbors to positions in the field that were several arcminutes away, resulting in very similar surface densities across large portions of the background. When paired with a method to quantify the significance of over-densities we found over-densities created by as few as five objects in the background would cover entire corners of the image.

2.4.3 Kernel Density Estimation

As previously discussed in this chapter, KDE smooths data by replacing the probability density function of an object with some predetermined function (or kernel), such as a Gaussian function. This effectively "spreads" each data point out in space. A strength of KDE is that the width of the kernel can be adjusted to the user's preference, meaning the output can be fine-tuned for substructure of varying sizes like the KNN technique. However, unlike the KNN which has a minimum coarseness to its fine-tuning (for instance, there is no way to calculate the surface density with the 9.5th nearest neighbor), there is no lower limit to the precision with which one may vary the kernel size.

Ultimately, we decided to estimate the local surface density using this method. Though both KDE and KNN are capable of highlighting substructure at different size scales, KNN tends to exaggerate over-densities in the sparsely populated regions of the images. While it is not expected that notable substructure will be found in the outer parts of the image, using KDE can allow a more robust characterization of substructure in the background.

.

References

D'Abrusco, R., Fabbiano, G., Strader, J., et al. 2013, ApJ, 773, 87.

D'Abrusco, R., Fabbiano, G., & Zezas, A. 2015, ApJ, 805, 26.

D'Abrusco, R., Cantiello, M., Paolillo, M., et al. 2016, ApJ, 819, L31.

Foreman-Mackey, D., Hogg, D. W., Lang, D., et al. 2013, PASP, 125, 306.

Graham, A. W. & Driver, S. P. 2005, PASA, 22, 118. doi:10.1071/AS05001

Kuzma, P. 2017, Extended Structures in Globular Clusters, Research School of Astronomy and Astrophysics, The Australian National University

Martin, N. F., de Jong, J. T. A., & Rix, H.-W. 2008, ApJ, 684, 1075.

Prugniel, P. & Simien, F. 1997, A&A, 321, 111

Silverman, B. W. 1986, Monographs on Statistics and Applied Probability, London: Chapman and Hall, 1986

Chapter 3

Searching For Substructure Within the Resolved Stellar Populations of M31 Dwarf Satellite Galaxies Lacerta I, Cassiopeia III, and Perseus I

In this chapter, we use existing wide-field CCD imaging data of three Andromeda dwarf satellites to examine the spatial distribution of their Red Giant Branch (RGB) stellar populations for substructure. The data for Lacerta I (hereafter Lac I) were previously presented in Rhode et al. (2017), who used it to characterize the spatial distribution of the RGB stars, estimate the galaxy distance, and investigate the stellar metallicity distribution. The data for Cassiopeia III (Cas III) and Perseus I (Per I) were obtained around the same time as the Lac I data but have not yet been included in a published study. Other works (e.g. Martin et al. 2013a,b; Rhode et al. 2017) have characterized these dwarf galaxies though only one has actively searched for substructure. Higgs et al. (2021) have examined Per I as part of a larger survey searching for substructure within isolated dwarf galaxies but no research of this nature has been published on Lac I and Cas III. This chapter seeks to explore these recently-discovered galaxies in the hope of uncovering features suggestive of their formation history.

3.1 Observations and Data Reduction

The observations of Lac I and Cas III were obtained on 1-3 October 2013 and those of Per I obtained on 29-31 October 2013 with the WIYN 3.5m telescope. The One

Degree Imager camera was used with a partially filled focal plane (pODI; Harbeck et al. 2014) with a main imaging area made up of a 3 x 3 array of Orthogonal Transfer Arrays (OTAs). The central OTA in pODI had a $\sim 24'$ x $24'$ field-of-view, with a pixel scale of $0.11''$.

For each galaxy several 600-700 s exposures were acquired with the Sloan Digital Sky Survey (SDSS) g and i filters. To fill the gaps between the OTAs and individual detectors that make up pODI, the telescope was dithered between exposures. Each image was evaluated and the highest-quality observations were stacked to obtain the best image quality possible for the final stacked image of each galaxy. After stacking, the total exposure time for Lac I was 6300 s in g (9 exposures) and 5400 s in i (9 exposures); the total exposure time for Cas III was 9000 s in g (13 exposures) and 5000 s in i (8 exposures); for Per I, the total exposure time was 5400 s in g (9 exposures) and 8400 s in i (14 exposures).

The stacked images were immediately transferred to the ODI Pipeline, Portal, and Archive (Gopu et al. 2014, ODI-PPA)[1] from WIYN. Individual exposures were processed using the QuickReduce pipeline (Kotulla 2014), which applied crosstalk and persistence corrections, subtracted the overscan signal, masked saturated pixels, corrected for non-linearity, applied bias, dark, flatfield, and pupil ghost corrections, as well as removed cosmic rays. Once through the QuickReduce pipeline, images were illumination-corrected with a night-sky flat, reprojected to a common pixel scale, and average-combined into a single, deep image for each filter. The edges of the images had a higher noise level as a consequence of the dither pattern providing incomplete coverage and so were trimmed, for a final image size of $\sim 20'$ x $20'$. For the stacked images of Lac I, the average Full Width at Half Maximum of the point spread function (FWHMPSF) is $0.84''$ in g and $0.74''$ in i; for Cas III, the mean FWHMPSF is $0.80''$

[1]The ODI Pipeline, Portal, and Archive (ODI-PPA) system is a joint development project of the WIYN Consortium, Inc., in partnership with Indiana University's Pervasive Technology Institute (PTI) and NSF's NOIRLab.

in both g and i filters; for the stacked images of Per I, the mean FWHMPSF value is $0.80''$ in g and $0.90''$ in i.

Per I is in an area of the sky that is included in the SDSS and therefore measurements of stars that appeared in both the final images of Per I and the SDSS photometry were used to determine zero points and color terms for the image. However, Lac I and Cas III are both outside of the SDSS footprint so these images were calibrated using exposures of standard star fields taken on a night with photometric conditions. As Cas III was observed later under non-photometric conditions, several modest-length exposures were taken to calculate the zero point offsets between the final, stacked Cas III images and the images from the photometric night. The calculated photometric coefficients were applied to all instrumental magnitudes measured using PSF photometry. Additionally, the extinction corrections for each source were calculated based on their position in the images using coefficients and maps of Galactic dust emission in Schlafly & Finkbeiner (2011) and Schlegel et al. (1998), respectively. Applying these values yielded dereddened g and i magnitudes and colors. The mean color excess for the Lac I field, Cas III field, and Per I field are $E(B-V) \sim 0.14$, $E(B-V) \sim 0.20$, and $E(B-V) \sim 0.15$ respectively.

3.1.1 Source Detection and PSF Photometry

Source detection and PSF-fitting photometry were performed on the final combined $g-$ and $i-$band images of Lac I, Cas III, and Per I using the DAOPHOT and ALLFRAME software (Stetson 1987, 1994). A set of $\sim$300 bright, unsaturated stars was used in each image to construct a PSF model. This model was then fitted to all sources in the images with peak counts greater than or equal to 3σ above the sky background level. The flux for each source was measured and then the resultant source catalog was culled (using specific DAOPHOT criteria that characterize the quality of the fit to the PSF model) in order to remove sources that were not genuinely point sources.

The final source catalogs for Lac I, Cas III, and Per I had 33,577 stars, 28,923 stars, and 15,263 stars, respectively.

Along with the photometric cuts, approximately one million artificial stars were injected into each set of images to determine the 50% completeness limits. To avoid crowding, the artificial stars were split amongst different experiments and were distributed evenly throughout each image across a range of magnitudes and colors based on our real sample. The same detection and photometric steps were then performed on the artificial stars. The overall color-averaged 50%-completeness limit for Lac I is reached at $g_0 = 25.6$ and $i_0 = 24.2$; for Cas III the overall color-averaged 50%-completeness limit is reached at $g_0 = 24.4$ and $i_0 = 23.6$; for Per I the overall color-averaged 50%-completeness limit is reached at $g_0 = 25.2$ and $i_0 = 24.3$.

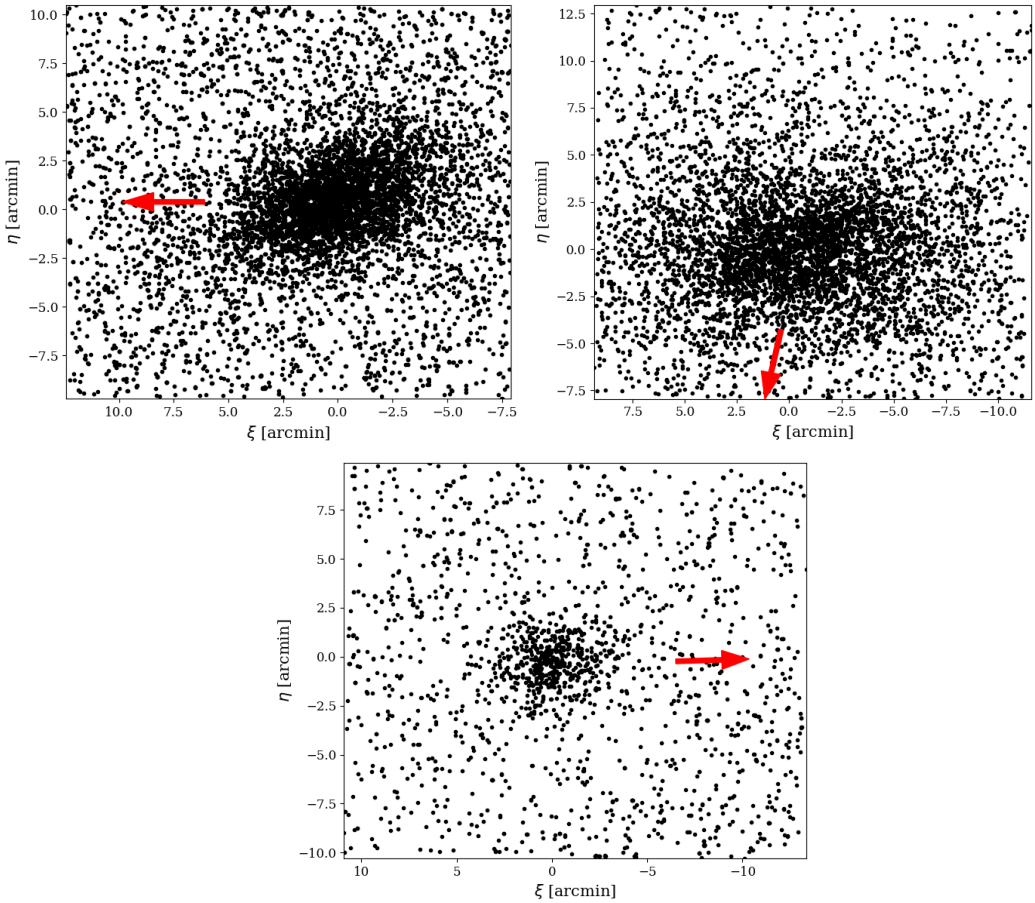

Figure 3.1 The positions of the RGB stellar populations of Lac I, Cas III, and Per I in standard coordinates. A red arrow is positioned to indicate the direction of M31 in each panel. The top-left panel shows Lac I, the top-right shows Cas III, and the bottom panel shows Per I.

Table 3.1. Details about the three Andromeda Dwarf Satellites Studied in this Dissertation.

Galaxy	Distance (kpc)	M31-centric Distance (kpc)	RA $(^\circ)^2$	Dec $(^\circ)^2$	Discovery Paper
Lacerta I	756^{+44}_{-28}	275 ± 7	344.567917	41.291111	Martin et al. (2013a)
Cassiopeia III	772^{+61}_{-56}	144^{+6}_{-4}	8.997500	51.559722	Martin et al. (2013a)
Perseus I	785 ± 65	374^{+14}_{-10}	45.348333	40.988333	Martin et al. (2013b)

[2]RA and Dec coordinates were sourced from the NASA/IPAC Extragalactic Database (NED)

The candidate Red Giant Branch (RGB) stars were selected based on their locations in a color-magnitude diagram (CMD) and these are the stars that make up the sample used to explore the structure and substructure of the galaxies. Figure 3.1 shows the positions of the RGB stars in the final, science-ready data set for each dwarf galaxy. Object positions have been converted to standard coordinates and the red arrows point towards M31. Lac I is shown in the top-left panel, Cas III in the top-right, and Per I in the bottom panel. The three galaxies and pertinent information are listed in Table 3.1.

3.1.2 Background Surface Density Estimation

In Rhode et al. (2017), the background surface density of Lac I was estimated to be 6.818 arcmin^{-2}. For the purposes of this analysis we adopt the same estimate. The background surface densities of Cas III and Per I were estimated by defining a set of rectangular regions near the edges of the two fields, as far away from the galaxies as possible. Cas III was more extended on the sky and covered much of the pODI field, so the regions chosen for it have a greater risk of including stars belonging to the galaxy. Therefore, it is reasonable to assume the background estimate for Cas III may be higher than the true value. The background surface density estimate for Cas III was 2.59 arcmin^{-2}. Using the same method for Per I we estimated the background surface density to be 3.66 arcmin^{-2}. However, as we will discuss in Section 3.3.3 the surface density of the background is not uniform, instead rising $\sim 5'$ from the galaxy center. This makes estimating the background surface density tricky, as naive placement of the rectangular regions could bias our result. In light of this, we decided to instead adjust the background surface density based on what value provided the best fit to the radial profile of Per I. We discuss this process in more detail in Section 3.3.3 but note here that we used a background surface density estimate of 3.30 arcmin^{-2}.

3.2 Methods

As discussed in Chapter 2, we use Maximum Likelihood Estimation (MLE) to derive four structural parameters (ellipticity, position angle, half-light radius, and Sersic index) along with the offset of the RGB stellar population from the adopted center of each galaxy (ΔRA, ΔDec). This technique uses a likelihood function to assume a model describing the spatial distribution of the stellar system and a Markov chain Monte Carlo (MCMC) algorithm to probe the parameter space for the best-fitting structural parameter values for that model. While the contamination surface density in each field could be left as a free parameter to be determined through MLE, we supply our own estimates, as described in the previous section, in order to reduce the number of free parameters the MLE must determine for the model. With a contamination surface density for each galaxy and a likelihood function derived, the spatial positions of the RGB population of the three dwarf galaxies could be fed into the MLE script where an MCMC python package (emcee; see Foreman-Mackey et al. 2013) would compute 30,000 steps with each step being a proposed set of structural parameters. If the proposed set of parameters are deemed to better fit the data they are saved and tested against the next set of proposed parameters in the next step. In this way, MLE slowly converges on a set of parameters that best fit the model to the data. For each set of parameters we took the median value of the saved proposals and estimated the uncertainty by calculating the 16th and 84th percentile values. In machine-learning algorithms the first steps are often ignored to allow the algorithm sufficient time to begin convergence and to minimize bias associated with the starting positions of the parameters. We found that ignoring the first 3000 steps was more than sufficient for convergence to begin, without the starting positions biasing the final median value.

3.2.1 Searching for Substructure in the Central Regions of the Galaxies

Past efforts to determine the structural parameters of dwarf galaxies have found success using exponential and Sersic models (see, e.g., Martin et al. 2013a,b; Rhode et al. 2017). In light of these previous successes we determine two sets of structural parameters for each galaxy using a MLE algorithm. The first set of parameters is calculated with an exponential model (corresponding to Sersic model with index $n = 1$) and a second set is determined with a Sersic model where we allow n to vary.

Once we have derived best-fitting parameters for the models that describe the spatial distributions of the stars, we then begin searching for substructure within the RGB population by dividing the field into a 30 by 30 cell grid and estimating the surface density at the center of each cell with our model. We then convert this surface density into the number of objects expected within each cell based on the area encompassed by a single grid cell. The expected number of objects in each grid cell represents the idealized comparison case (i.e., an unperturbed dwarf) and so we can compare the model estimates to the data; deviations in the measured surface density from what the model predicts would indicate the presence of a feature, possibly due to a merger or accretion event. The stellar data for the dwarfs was binned into the same 30 by 30 grid used for the model estimates. The expected number of objects in each grid cell was then subtracted from the number of RGB stars in that same cell. The uncertainty in our result is Poissonian in nature and so we determine the significance of any individual residual by dividing the difference by the square root of the number of stars in each grid cell. This method is repeated for each galaxy, adopting an exponential profile and a more general Sersic profile.

It should be noted that this method was designed with the intention of probing the inner regions of the galaxies where densities will be high and bins can be expected to reliably contain tens of points. Attempts to derive significance in deviations from

the model outside of the main body of a galaxy are likely to fail as the data becomes more sparse. If a bin is populated with only a handful of stars the relative uncertainty in the residual is too large to make claims about the result. For this reason, we restrict ourselves to the inner two half-light radii of each galaxy when searching for substructure in this manner.

3.2.2 Searching for Substructure Beyond 2 Half-Light Radii Using Residuals

Beyond two half-light radii the data become too sparse to bin and subtract the estimated number of objects in each grid cell. At these radii the expected number of objects would be less than one and many grid cells would be completely empty or have a single object within them. Instead of lowering the resolution by increasing the bin size, we utilize Kernel Density Estimation (KDE) to generate a local surface density estimate of the RGB population across the field in a 100 by 100 grid. Outside of the main body of the galaxy the surface density should be dominated by random objects in the background and foreground, so rather than use models, a simple background surface density estimate is utilized to search for substructure in this region.

In order to identify deviations of the surface density in the background and quantify the significance of those deviations we generate the total number of background objects that should exist in the image based on the background surface density and scatter them randomly across the field. Then KDE is used to estimate the surface density across the field in a 100 by 100 grid. The average surface density of the grid cells is calculated and converted into an expected number of objects per cell. The KDE surface density estimates of the RGB population are likewise converted to an estimate of the number of objects in each grid cell. Residuals are then created by subtracting the estimated number of background objects per cell from the estimated number of objects in each cell. Dividing by the square root of the estimated number

of background objects per cell quantifies the significance of any deviations in the data.

This method is guaranteed to flag the portion of the galaxy inside two half-light radii as a significant over-density when compared to the background. To avoid this we flag any over-density $> 4\sigma$ above the background as part of the main body of the galaxy. A significant over-density that is well separated from the galaxy can be readily identified as a possible fingerprint of substructure.

3.3 Results for Each Galaxy

In this section, we discuss three points concerning the structural properties of each galaxy. First we compare our estimated structural parameters to past studies to see how well our findings agree and check how well our models fit the radial profile. Next we discuss the results of our search for substructure within the inner two half-light radii of the galaxy using the method described in Section 3.2. Finally, we search the field beyond two half-light radii and discuss possible substructures within this region for the three galaxies.

3.3.1 Lacerta I

Since we are using the same data set and a similar method to those used in the Rhode et al. (2017) study, we should expect our findings to be similar. Comparing our results shown in Table 3.3.1 to those reported in their study, we find that our best fitting parameters are in agreement in all cases.

Figure 3.2 shows the surface density of the Lac I RGB stellar population as a function of elliptical radius (open diamonds) along with the exponential profile (solid black line) and background surface density level (dashed black line). The left panel presents a comparison of the exponential fit and the right panel a Sersic fit ($n = 0.83$). Both sets of structural parameters produce fits that closely mirror the data beyond $\sim 1'$ but fail to accurately reproduce the surface densities in the innermost region of

Table 3.2. The estimated structural parameters of the Andromeda dwarf satellite galaxy, Lacerta I as well as the spatial offset of the RGB stellar population from the adopted center. Structural parameters were estimated using an MLE algorithm to fit a general Sersic and exponential function to the RGB stellar population.

Parameters	Lacerta I	Lacerta I ($n = 1$)
Ellipticity (ϵ)	0.41 ± 0.01	0.40 ± 0.01
Position Angle (θ) [$^\circ$]	-64 ± 1	-63 ± 1
Half-Light Radius (r_h) [$'$]	3.18 ± 0.05	3.13 ± 0.05
Sersic Index (n)	0.83 ± 0.03	–
ΔRA [$'$]	-0.27 ± 0.04	-0.28 ± 0.04
ΔDec [$'$]	0.48 ± 0.03	0.48 ± 0.03

the galaxy. The exponential fit overestimates the central surface density by $\sim 1\sigma$. This may be due to stellar crowding in the dense inner regions of the galaxy and/or to the presence of bright Galactic foreground stars that prevent us from detecting Lac I stars in those regions. Likewise the Sersic fit underestimates the surface density at elliptical radii $> 0.7'$, possibly over-compensating for lower than expected surface densities within the central region. In both cases the fits are largely representative of the radial profiles even with minor deviations in the central region.

3.3.1.1 Residuals within the Inner Two Half-Light Radii of the Galaxy

As detailed in Section 3.2, we created maps of the residuals when comparing surface densities of the inner two half-light radii of each galaxy to the surface densities our models predict. We begin this analysis with the Lac I residuals in Figure 3.3 where the structural parameters used were those obtained with the exponential profile. There appear to be a string of over-densities running upwards just west of the center of the image. These over-densities range from 2.5 to 3σ above the model expectations. The center of the galaxy also has an under-density, likely a result of the crowding and foreground star removal mentioned previously.

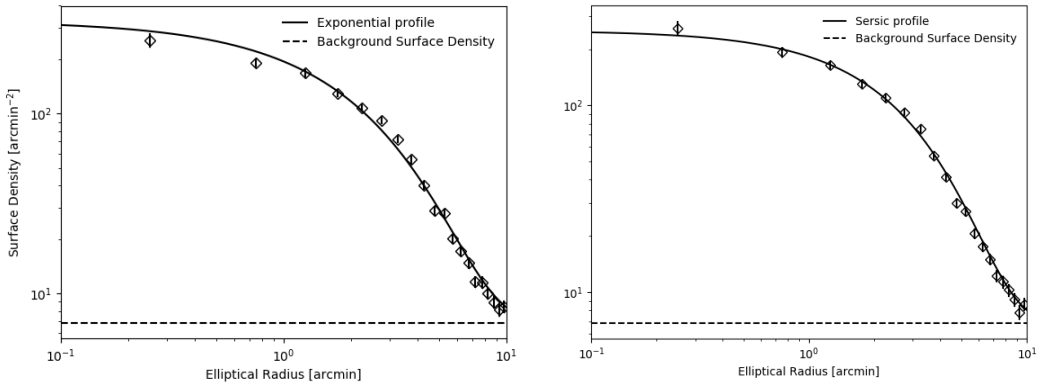

Figure 3.2 The surface density of the RGB stars in Lac I as a function of elliptical radius. The solid black line is the best-fitting function using the structural parameters derived from MLE. Open diamonds indicate the surface density of each bin with uncertainties overlaid. The dashed black line indicates the level of the background surface density. The left panel compares the exponential fit and the right panel compares the Sersic ($n = 0.83$) fit.

Figure 3.4 shows the residuals for Lac I field when the Sersic index was allowed to vary in the model. The under-density within the center of the galaxy has diminished, likely because our MLE algorithm found a lower Sersic index that can better account for the slightly depressed surface density in this region. The chain of over-densities along the west side still exists, with significances varying between 2-3σ. Less significant under-densities to the north and to the southeast of center have expanded in size but lack the same cohesion seen in the chain of over-densities, suggesting they may be fluctuations rather than substructure.

Ultimately, the residuals suggest that there is a portion between one and two half-light radii of the Lac I galaxy with an abundance of RGB stars that is not accounted for by the models. That these over-densities are not located sporadically across the field but rather are connected by less significant over-dense regions, suggests that this chain of over-densities may be a coherent substructure, possibly even the result of a tidal interaction or minor merger.

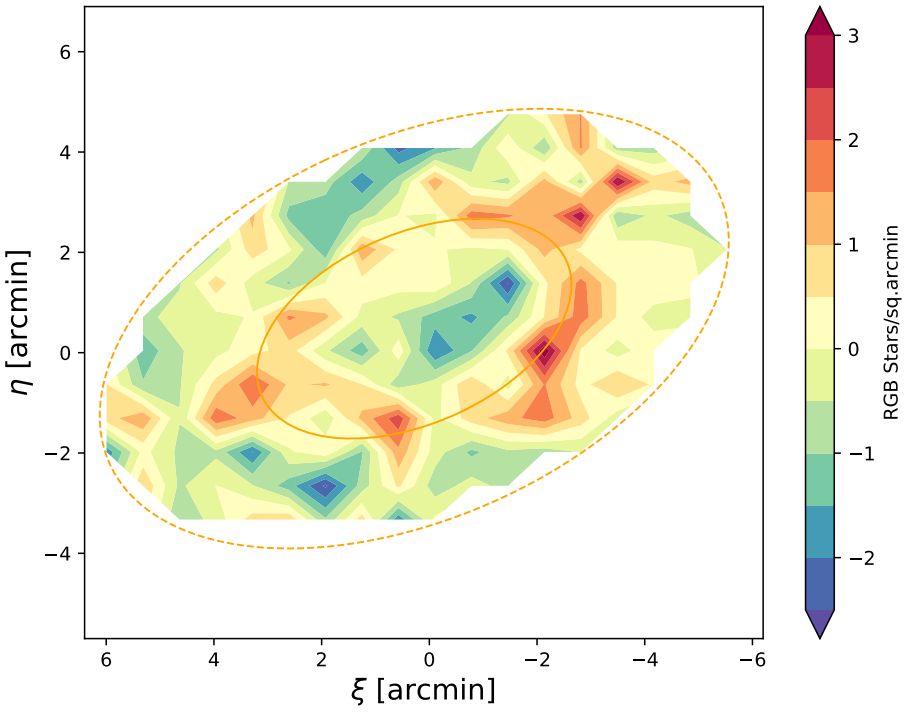

Figure 3.3 The residuals for the inner two half-light radii of Lac I with parameters obtained by MLE with the Sersic index, n, held fixed at one. The solid orange ellipse demarcates the half-light radius, with the dashed orange line indicating two half-light radii and the point where our model stops. There is a chain of modestly significant ($\sim$2.5-3σ) over-densities that run from the west side of the galaxy towards the top near the half-light radius. There is a under-density present within the center which is likely due to crowding or the removal of foreground stars depressing the surface density. In this figure, north is up and east is to the left.

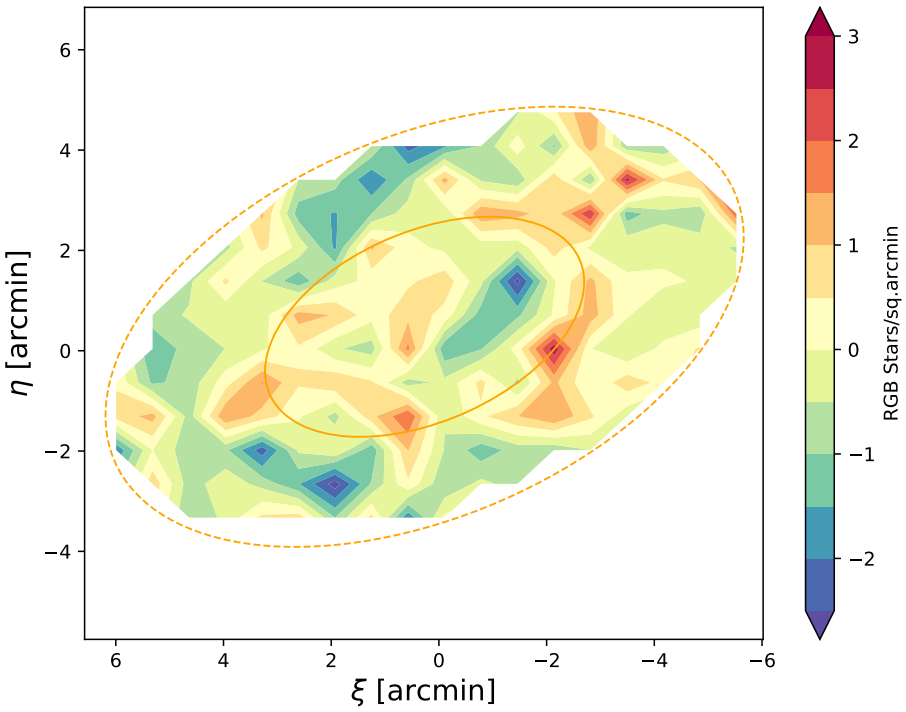

Figure 3.4 The residuals for the inner two half-light radii of Lac I with parameters obtained by MLE with the Sersic index allowed to vary ($n = 0.77 \pm 0.03$). The solid orange ellipse marks the half-light radius of the galaxy and the dashed orange ellipse two half-light radii. The chain of over-densities along the west side of the galaxy are still present, although weaker. In this figure, north is up and east is to the left.

3.3.1.2 Residuals Beyond Two Half-Light Radii

The residuals of the Lac I field are shown in Figure 3.5. The white lines are iso-density contours that highlight areas where the density reaches 1σ, 2σ, or 3σ above the background surface density. Densities $> 2\sigma$ above the background only appear around the main body of the galaxy, with little deviation in shape. The field is populated with 1σ over-densities that are unconnected to the galaxy itself but these are likely to be fluctuations in the background rather than substructure. However, there appears to be a $1 - 2\sigma$ filament towards the southeast of the galaxy. This filament is part of the 1σ contour encompassing the galaxy itself, which suggests that it could be an extended portion of the Lac I RGB star population rather than merely a fluctuation in the background. Although the surface densities are only between $1-2\sigma$ above the field surface density, this filament could be a coherent structure that warrants further study of the stars in this region.

3.3.2 Cassiopeia III

Table 3.3.2 shows our estimated structural parameters for Cas III. The study done by Martin et al. (2013a) found an ellipticity ($\epsilon = 0.5 \pm 0.09$) and half-light radius ($r_h = 6.5^{+1.2}_{-1.0}$ arcmin) that both significantly differ from ours. These differences may be due to the fact that Cas III fills a large portion of the field-of-view in our images. Muñoz et al. (2012) found that for an imaging study of a resolved dwarf galaxy to yield reliable structural parameters, the field-of-view of the images must be more than three times larger than the half-light radius of the dwarf. Cas III has such a large r_h that our WIYN pODI do not quite meet this criterion. In order to test our assumption that inadequate spatial coverage was impacting our derived structural parameters, we generated a set of data with an extent and spatial distribution that matched those reported by Martin et al. (2013a). When presented with this set of generated data,

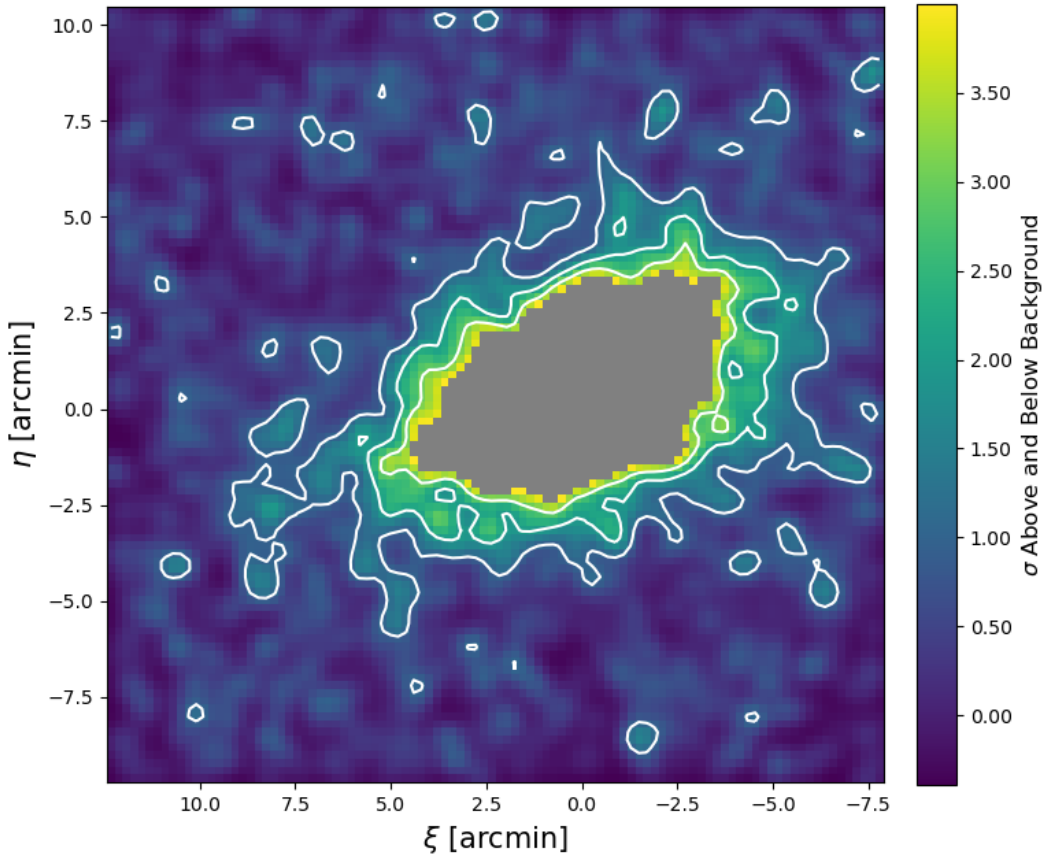

Figure 3.5 The residuals in the Lac I field where the galaxy profile no longer dominates. Over-densities above 4σ are masked in gray and considered the main body of the galaxy. The white contours encompass 1σ, 2σ, and 3σ regions. Lac I has many low-significance filaments reaching from the main body of the galaxy, particularly on towards the southeast, partially in the direction of M31. North is up and east is to the left.

Table 3.3. The estimated structural parameters of the Cassiopeia III Andromeda dwarf satellite as well as the offset of the RGB stellar population from the adopted center. Structural parameters were estimated using an MLE algorithm to fit a general Sersic and exponential function to the RGB stellar population.

Parameters	Cassiopeia III	Cassiopeia III ($n = 1$)
Ellipticity (ϵ)	0.30 ± 0.01	0.30 ± 0.01
Position Angle (θ) [$^\circ$]	91 ± 2	91 ± 2
Half-Light Radius (r_h) [$'$]	4.63 ± 0.06	4.73 ± 0.09
Sersic Index (n)	0.59 ± 0.02	–
ΔRA [$'$]	-0.54 ± 0.07	-0.49 ± 0.06
ΔDec [$'$]	-0.02 ± 0.05	0.02 ± 0.05

our MLE algorithm returned the expected set of structural parameters, that is those matching the Martin et al. (2013a) study. We then generated a new set of data with a spatial distribution that matched those reported by Martin et al. (2013a) but required that it have the same number of objects and fall within the same field of view as our Cas III data. When the new data were fed to our MLE algorithm it returned a half-light radius of $r_h = 4.6' \pm 0.07$ and an ellipticity of $\epsilon = 0.40 \pm 0.01$. The half-light radius was reduced by two arcminutes and there was a difference of 0.1 in the measured ellipticity due to the restrictions we imposed on the field of view. While this test does not fully account for the differences between our measured ellipticity and that presented in Martin et al. (2013a), the differences in the half-light radius can be fully explained by the smaller field of view of our observations.

The fits for Cas III, as shown in Figure 3.6, are markedly worse than those for Lac I. The central $\sim 3-4'$ are not well-fitted by a Sersic/exponential function, where the surface density should decrease monotonically. It seems likely that overcrowding within the central $3'$ of the galaxy is at least partially at fault for this. However, the exponential fit appears to reproduce well the radial surface density profile between $3 - 8'$, though it underestimates the data beyond that point. The Sersic fit with

$n = 0.57$ appears to better reproduce the inner ($< 3'$) and outer ($> 8'$) regions of the surface density profile but overestimates the area in between.

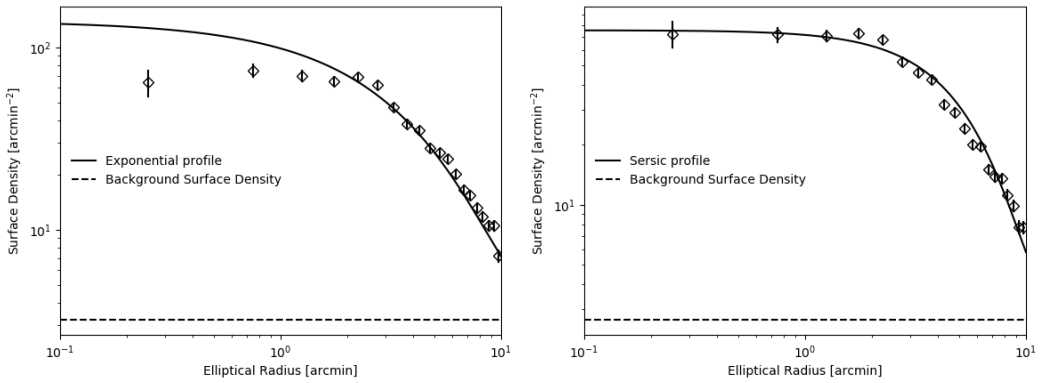

Figure 3.6 The surface density (open diamonds) of Cas III as a function of elliptical radius. The fit (solid black line) is calculated using the structural parameters derived from MLE. The background surface density level is indicated by the dashed black line. The left panel illustrates an exponential fit and the right panel compares the Sersic fit where $n = 0.57$.

These findings suggest that any substructure found in Cas III using this method will have to be considered with a degree of caution. Beyond $\sim 3'$ the exponential fit is reasonable enough to warrant inspection of the residuals, but the Sersic fit is unlikely to yield results in which we can be confident.

3.3.2.1 Residuals within the Inner Two Half-Light Radii of the Galaxy

Our analysis of Cas III was hampered by over-crowding extending a few arcminutes around the center of the galaxy. This crowding, and therefore under-counting of the RGB stars within the area, had a drastic effect on the Sersic index, n, returned by the MLE process. However, we also include the residuals obtained with the MLE algorithm where the Sersic index is left free for completeness. The crowded region is shown as a gray oval encompassing the inner 3 arcminutes of the galaxy residuals in both Figures 3.7 and 3.8.

In Figure 3.7, there are two over-densities just outside the masked portion in the

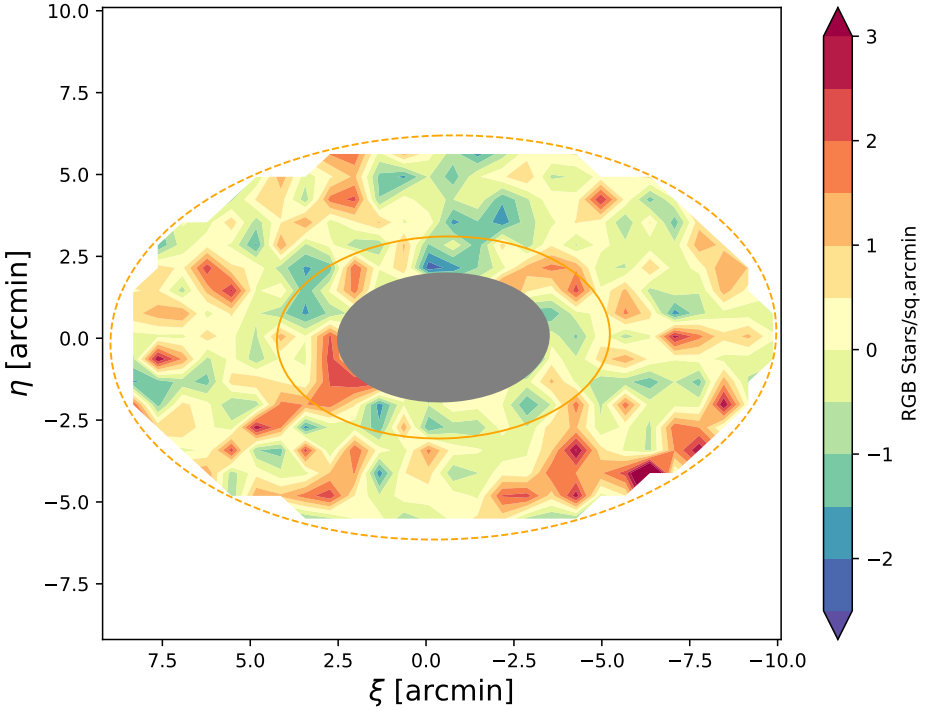

Figure 3.7 The residuals of the inner 2 half-light radii of Cas III with the solid orange ellipse and dotted orange ellipse denoting 1 and 2 half-light radii respectively. The central 3′ of the galaxy have been masked with a gray ellipse due to significant crowding in the region disrupting the fit. Just beyond this crowded region there exist two over-densities to the northwest and southeast. Due to the crowding it is impossible to tell if these two over-densities are a single coherent substructure or if their perceived alignment is a trick of the eye. In this figure, north is up and east is to the left.

northwest and southeast directions. From the size and shape of the two over-densities it is easy to see the possibility that they could connect within the overcrowded region, creating a coherent structure spanning the entirety of the solid-orange ellipse that denotes the half-light radius of Cas III. Such a structure would resemble the accreted remnants of dwarfs within larger systems, such as those exhibited in the Stellar Tidal Stream Survey (Martinez-Delgado et al. 2021). If this is an actual coherent structure, the simplest explanation might be that it is caused by an interaction with the Andromeda galaxy. Unfortunately, whether this is one stream or two separate over-densities is speculation, though future work that focuses on measuring the

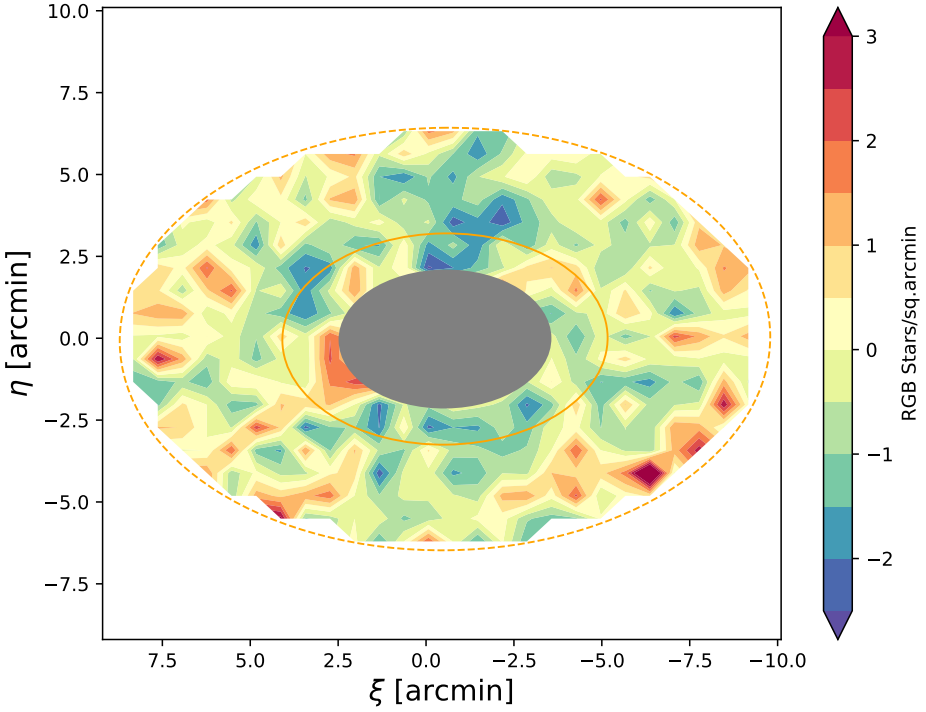

Figure 3.8 Residuals of Cas III out to 2 half-light radii with the solid orange ellipse and dotted orange ellipse denoting 1 and 2 half-light radii respectively . The inner 3′ have been masked due to significant crowding in the region. Structural parameters for the model were obtained while leaving n free ($n = 0.59 \pm 0.02$). The over-densities along the northwest and southeast are still visible but less significant. There exists a 3σ over-density along the southwest side of the 2 half-light radii ellipse, though it may be an artifact due to the poor fit. In this figure north is up and east is to the left.

metallicities and radial velocities of the RGB stars within these over-dense regions may help shed light on this topic.

In both Figures 3.7 and 3.8 there appears to be a structure of minor ($\sim$2-3σ) significance along the southwest side of the two half-light radius ellipse. This could indicate a deposit of RGB stars within the region from a tidal event. However, given the poor fits for Cas III, this should be considered with due caution as it may be an artifact of the MLE process.

3.3.2.2 Residuals Beyond Two Half-Light Radii

In Figure 3.9 the residuals of Cas III are shown with white iso-density contours encircling surface densities 1σ, 2σ, and 3σ above the background surface density. Surface densities greater than 4σ above the background are shaded gray and considered part of the galaxy. The iso-density contours match the general shape of the galaxy, showing no obvious tidal features within the background. However, to the southwest of the galaxy there exists a $> 4\sigma$ over-density encompassed by the 2σ contour but otherwise isolated from the rest of the regions with surface densities $> 3\sigma$. This is likely the same over-density seen in the southwest corner of Figure 3.7. No masking exists in this area that can account for the relative isolation of this over-density and since the method to identify substructure in the background is independent of the galaxy models, the crowding in the central $3'$ should have no bearing on these results.

3.3.3 Perseus I

The structural parameters for Per I have most recently been estimated using MLE in Higgs et al. (2021). Comparing their results to ours (reported in Table 3.4), we find ourselves in agreement over all shared structural parameters (ϵ, θ r_h, and n) for Per I.

We briefly mentioned in Section 3.1.2 that the background surface density was not uniform and that attempting to make a background surface density estimate with the same method used for Cas III would likely end up with a biased result. Instead we adjusted the background surface density estimate between 3 and 3.75 arcmin^{-2} in increments of 0.05. Each time the estimate was adjusted, the MLE algorithm found a new set of best fitting parameters for that estimate. We then took the sum of the squared residuals (SSR) between the surface density values of our radial profile and the surface density estimated by our model at that radius. The value of the SSR

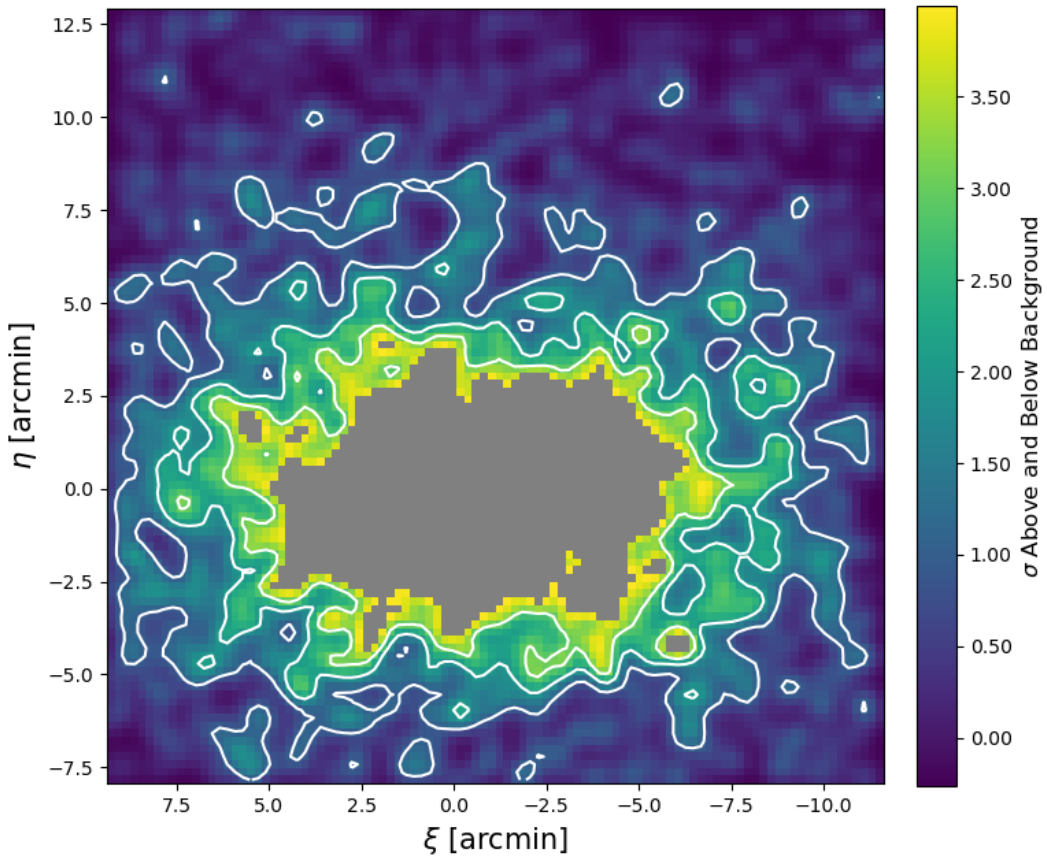

Figure 3.9 The residuals of the Cas III field. Gray masks are applied to surface densities $> 4\sigma$ above the background level. White iso-density contours have been added that correspond to surface densities 1σ, 2σ, and 3σ above the background surface density. The field is filled primarily with low-significance filaments connected to the main body of Cas III. There is a region to the southwest with surface densities $> 4\sigma$ above the background that is not directly connected to the rest of the main body of Cas III. This is likely the same over-density seen in the southwest corner of Figure 3.7 In this figure, north is up and east is to the left.

Table 3.4. The estimated structural parameters of the Cassiopeia III Andromeda dwarf satellite as well as the offset of the RGB stellar population from the adopted center. Structural parameters were estimated using an MLE algorithm to fit a general Sersic and exponential function to the RGB stellar population.

Parameters	Perseus I	Perseus I ($n = 1$)
Ellipticity (ϵ)	$0.09 \pm +0.06$	0.09 ± 0.06
Position Angle (θ) [$^\circ$]	-58^{+25}_{-21}	-59^{+23}_{-20}
Half-Light Radius (r_h) [$'$]	1.39 ± 0.07	$1.40^{+0.07}_{-0.06}$
Sersic Index (n)	0.7 ± 0.1	–
ΔRA [$'$]	-0.02 ± 0.06	-0.04 ± 0.06
ΔDec [$'$]	-0.22 ± 0.06	-0.21 ± 0.06

was recorded for each adjustment of the background surface density and the estimate that produced the smallest SSR was used with the corresponding best fit parameters reported. In this case, that estimate was 3.30 arcmin^{-2}.

The fits (shown in Figure 3.10) are reasonable, with the most notable deviation occurring at $0.25'$ in the exponential fit. Here the radial profile appears to flatten, deviating from estimate of the exponential model. This may be indicative of a feature near the very center of Per I but the possibility that an exponential fit is simply not well-suited here exists as well. This possibility is strengthened by the how well the Sersic fit describes the radial profile, including the central region.

3.3.3.1 Residuals within the Inner Two Half-Light Radii of the Galaxy

The residuals for Per I show no strong evidence for substructure. Figure 3.11 shows the residuals with the model parameters from the exponential profile. The strongest over-density occurs near the 2 half-light radii ellipse (dashed-orange line) south of the galaxy center and has a significance between $\sim$2.5-3σ. Nothing else within the galaxy shows the same level of significance and there does not appear to be any coherence to the residuals. Figure 3.12 shows the residuals of Per I when n is allowed

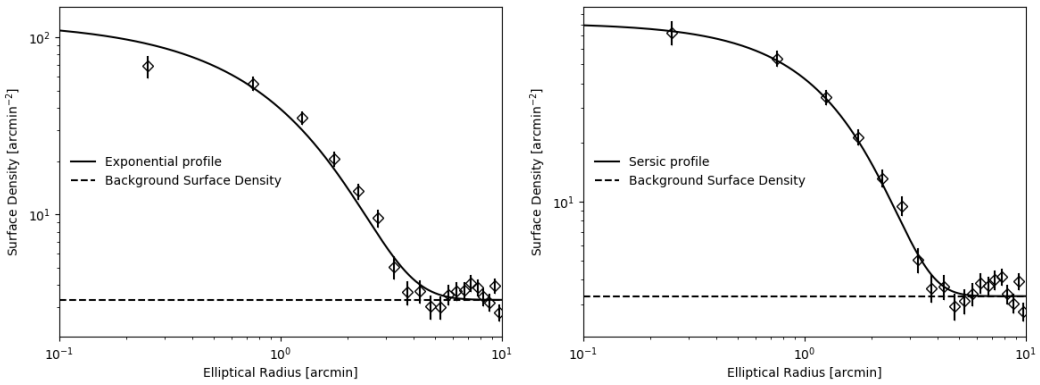

Figure 3.10 The surface density (open diamonds) of Per I as a function of elliptical radius. The fit (solid black line) is calculated using the structural parameters derived from MLE. The background surface density level is indicated by the dashed black line. The left panel illustrates an exponential fit and the right panel compares the Sersic fit where $n = 0.61$.

to vary in the model parameters. In this case the primary over-density south of the galaxy maintains a peak significance of $\sim 2.5\sigma$ but the area covered is smaller and less significant. There is still no coherence to the over-densities in the region with significances $> 2\sigma$. The residuals presented in Figure 3.11 and Figure 3.12 paint a picture of a relatively pristine dwarf galaxy. As mentioned in its discovery paper (Martin et al. 2013b), Per I lies $\sim 28^{\circ}$ distant ($\sim$ 374 kpc) from M31. While bound to Andromeda it may be that Per I has not had strong enough interactions with the galaxy or its satellites to generate the type of tidal features our methods would reveal.

3.3.3.2 Residuals Beyond Two Half-Light Radii

The residuals of the Per I field in Figure 3.13 are marked with white iso-density contours. The field is filled with fluctuations at the 1σ level that appear to be random, with no coherent substructure. However, along the outer edges of the Per I galaxy there exists a very slight extended shelf along the northwest side and a small, 2σ filament extending south away from the galaxy. These may be indicative of substructure and warrant further study of the stars in these regions but it may also be that deeper

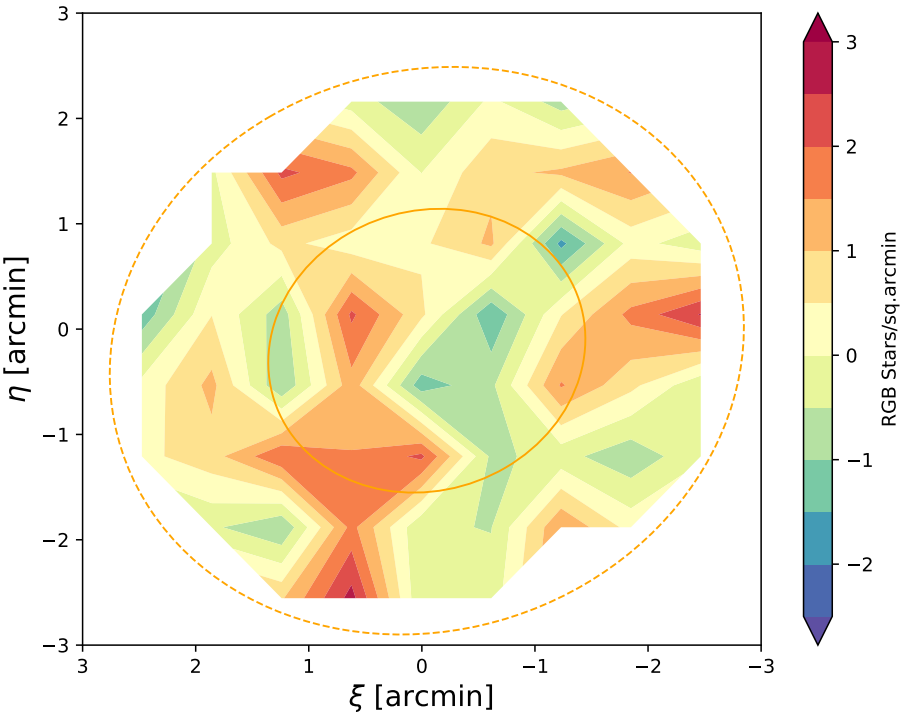

Figure 3.11 Residuals of Perseus I out to 2 half-light radii with the solid orange ellipse and dotted orange ellipse denoting 1 and 2 half-light radii respectively. Structural parameters for the model were obtained while holding $n = 1$. There is an over-density south the galaxy center with a peak significance of 2.5-3σ but the lack of other features suggests this may be a fluctuation in the surface density rather than a tidal feature. In this figure north is up and east is to the left.

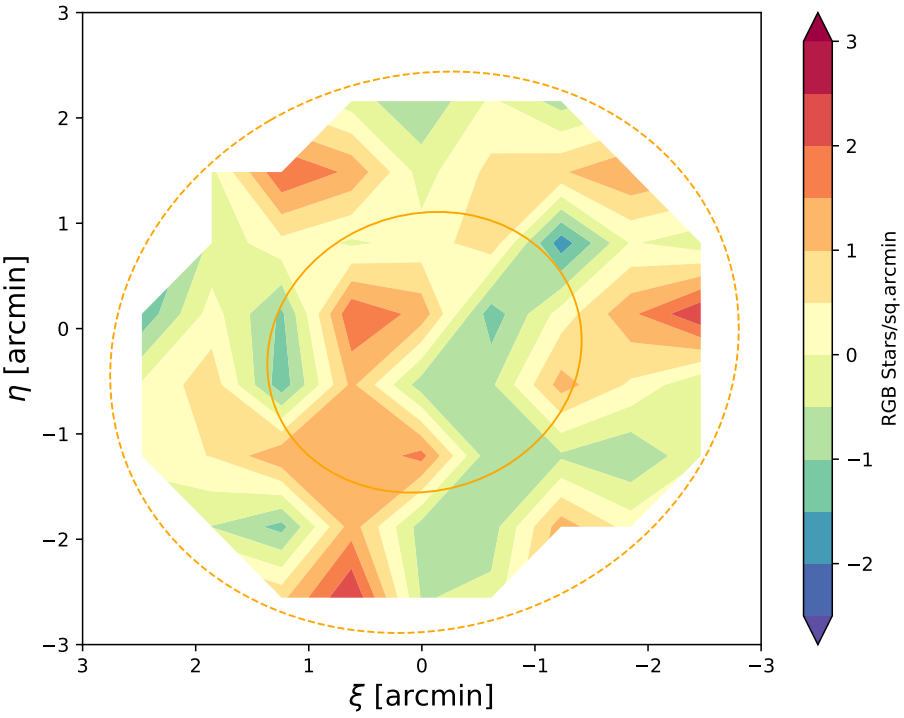

Figure 3.12 Residuals of Perseus I out to 2 half-light radii, the solid orange ellipse and dotted orange ellipse denoting 1 and 2 half-light radii respectively, with structural parameters for the model obtained with n allowed to vary ($n = 0.8 \pm 0.1$). Similarly to the $n = 1$ case, there is an over-density south of the center of the galaxy with a peak significance between 2.5 and 3σ but no other features of note. Lack of any coherent over/under-densities suggests that any substructure within the galaxy's RGB population is too subtle to be spotted with our data. North is up and east is to the left in this figure.

photometry is needed to uncover evidence of any interactions in the past history of this galaxy.

3.4 Conclusions

In this chapter we set out to characterize the structural parameters of three dwarf satellite galaxies (Lac I, Cas III, and Per I) that orbit the Local Group spiral galaxy M31, as well as to probe the galaxies' respective RGB stellar populations for substructure. Using a technique involving MLE we estimated the ellipticity, position angle, half-light radius, Sersic index, and central galaxy coordinates for each dwarf galaxy (see Tables 3.3.1, 3.3.2, and 3.4) and two corresponding models were created using a Sersic and exponential function. These models were then compared to the data and residuals were used to identify possible substructure within the central two half-light radii of each galaxy. Estimation of the background surface density in each field was used to search for substructure beyond two half-light radii.

Within two half-light radii of Lac I we found a string of over-densities along the northwest side with significances between $2.5 - 3\sigma$. The coherence of these over-densities indicates a possible substructure. Beyond two half-light radii there is little extended structure to be seen. A low-significance filament appears to stretch from Lac I towards the southeast, at least partially in the direction of M31; however, other structures of note are not identifiable in the region.

Cas III also shows possible evidence of an over-density within one half-light radius of the galaxy center. Two over-densities exist along the northwest and southeast. Due to crowding within the central $3'$ it is impossible to say for certain whether these are two isolated over-densities or one coherent over-density. In future work, if the crowding can be avoided, these over-densities are a promising lead in the search of substructure within the dwarf galaxy. Beyond two half-light radii, no coherent substructure can be seen. Examination of the velocities and metallicities of the RGB

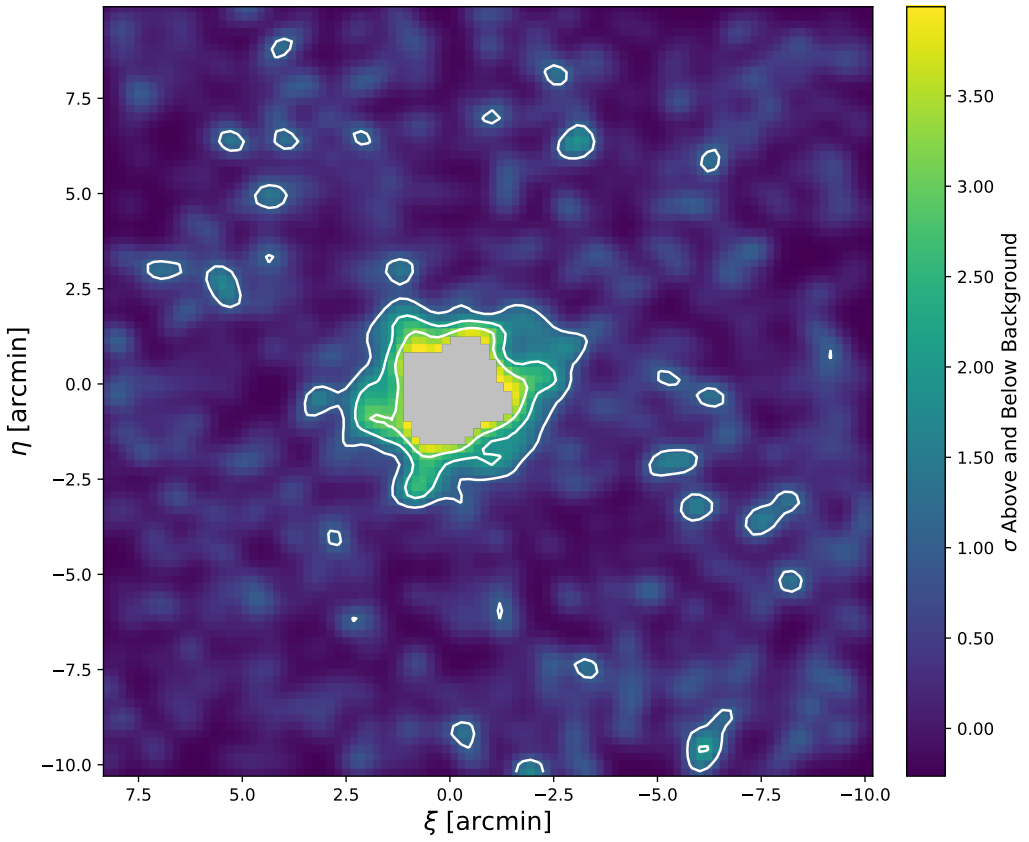

Figure 3.13 The residuals of the Per I field. The white iso-density contours correspond to surface densities 1σ, 2σ, and 3σ above the mean background surface density. A gray mask has been applied to cells with surface densities $> 4\sigma$ above the background surface density as they are considered part of the galaxy. There appears to be a small $\sim 2\sigma$ filament extending towards the southeast and an extended, 1σ shelf along the northwest. Otherwise the field is characterized by sporadic 1σ over-densities that are likely fluctuations within the background. North is up and east is to the left in this figure.

stars projected onto these over-densities may yield answers as well. As mentioned in Section 3.1, the background surface density may be over-estimated and so it is possible that potential substructure is buried in the field.

Per I shows no evidence for substructure within two half-light radii and little evidence beyond. A single over-density exists approximately two half-light radii south of the galaxy center. This over-density is isolated, suggesting it may be a fluctuation rather than a substructure within the galaxy. In the background, Per I appears relatively unperturbed except two features: a small, 2σ filament extends south from the galaxy and an extended shelf exists at the 1σ-level to the northwest, in the direction of M31. The lack of prominent substructure within and around the galaxy seems consistent with the galaxy's relative isolation.

References

Foreman-Mackey, D., Hogg, D. W., Lang, D., et al. 2013, PASP, 125, 306.

Gopu, A., Hayashi, S., Young, M. D., et al. 2014, Proc. SPIE, 9152, 91520E.

Harbeck, D. R., Boroson, T., Lesser, M., et al. 2014, Proc. SPIE, 9147, 91470P.

Higgs, C. R., McConnachie, A. W., Annau, N., et al. 2021, MNRAS, 503, 176.

Kotulla, R. 2014, Astronomical Data Analysis Software and Systems XXIII, 485, 375

Martin, N. F., Slater, C. T., Schlafly, E. F., et al. 2013, ApJ, 772, 15.

Martin, N. F., Schlafly, E. F., Slater, C. T., et al. 2013, ApJ, 779, L10.

Martinez-Delgado, D., Cooper, A. P., Roman, J., et al. 2021, arXiv:2104.06071

Muñoz, R. R., Padmanabhan, N., & Geha, M. 2012, ApJ, 745, 127.

Rhode, K. L., Crnojević, D., Sand, D. J., et al. 2017, ApJ, 836, 137.

Schlafly, E. F. & Finkbeiner, D. P. 2011, ApJ, 737, 103.

Schlegel, D. J., Finkbeiner, D. P., & Davis, M. 1998, ApJ, 500, 525.

Stetson, P. B. 1987, PASP, 99, 191.

Stetson, P. B. 1994, PASP, 106, 250.

Chapter 4

Substructure in the Globular Cluster Populations of the Virgo Cluster Elliptical Galaxies M84 and M86

In this chapter, we make use of existing wide-field CCD imaging data to search for evidence of substructure and galaxy interactions in the GC system of the Virgo Cluster elliptical galaxy M86 (NGC 4406) and the neighboring elliptical galaxy M84 (NGC 4374). Previous efforts have been made to study the substructure present within the central few arc minutes of the M86 GC system (D'Abrusco et al. 2015) and across the Virgo Cluster as a whole (Durrell et al. 2014). The spatial coverage of our data falls in between these two past works; our images include the two massive elliptical galaxies along with several other low-mass galaxies located at similar distances. Our study is intended to explore whether the globular cluster systems of the galaxies in the M86 field show any evidence for interactions between the galaxies and their cluster populations. Theoretical studies predict that environmental effects due to a galaxy cluster tidal field and galaxy interactions can significantly affect the morphological and kinematic properties of GC systems (e.g. Ramos et al. 2015), strip some GCs from their original host galaxies (e.g Forte et al. 1982; Muzzio et al. 1984; Ramos-Almendares et al. 2018, 2020), and produce intracluster GC populations (e.g. Yahagi & Bekki 2005; Bekki & Yahagi 2006, 2009). The goal here is to carefully

[1]This chapter has paragraphs based on the paper Lambert, R.A., Rhode, K.L., Vesperini, E. 2020, ApJ, 900, 45., "Substructure in the Globular Cluster Populations of the Virgo Cluster Elliptical Galaxies M84 and M86."

search for signatures of these processes in our observational data.

4.1 Observational Data and Globular Cluster Candidates List

To investigate substructure in the globular cluster systems of M86 and M84 and the surrounding region, we used the same imaging data that were originally presented in Rhode & Zepf (2004). The goal of the Rhode & Zepf (2004) study was to quantify the global properties - i.e., the total number of globular clusters, along with the specific frequency, radial distribution, color distribution, and color gradient - of the globular cluster system of M86 and a few other giant early-type galaxies. The images of the M86 field were obtained in March 1999 with the Mosaic imaging camera on the Mayall 4-meter telescope at Kitt Peak National Observatory[2], as part of a wide-field multi-color optical survey of the globular cluster systems of a sample of several spiral, S0, and elliptical galaxies (e.g., Rhode & Zepf 2001, 2003, 2004; Rhode et al. 2007). A $\sim 36'$ x $36'$ area around M86 was imaged for a total integration time of 3900 sec in B, 2700 sec in V and 2100 sec in R. A detailed description of how the Mosaic images were processed and calibrated is given in the original Rhode & Zepf (2004) paper. The pixel scale of the final science images we used is $0.26''$ pixel^{-1} and the full width half maximum of the point spread function (FWHMPSF) is $\sim 0.98''$, $1.1''$, and $1.2''$ in the B, V, and R images, respectively.

In the original study, Rhode & Zepf (2004) found that M86 hosts a population of $\sim$2900 globular clusters that extends $\sim$80 kpc from the galaxy center. The globular cluster system shows at least two peaks in the $B - R$ color distribution as well as a detectable radial color gradient that arises because the red population of globular clusters is more centrally concentrated than the blue population. Later, Hargis &

[2]Based on observations at Kitt Peak National Observatory at NSF's NOIRlab, which is managed by the Association of Universities for Research in Astronomy (AURA) under cooperative agreement with the National Science Foundation. The authors are honored to be permitted to conduct astronomical research on Iolkam Du'ag (Kitt Peak), a mountain with particular significance to the Tohono O'odham.

Rhode (2014) used the same Mosaic imaging data to examine the spatial distribution of the globular cluster system of M86 and compare it to the galaxy's light distribution. They found that the diffuse galaxy light and the globular clusters had similarly flattened, elongated distributions. The total globular cluster population, as well as the blue and red subpopulations, have nearly identical azimuthal distributions as the galaxy itself, with ellipticities $\epsilon \sim 0.4$ and position angles of ~ -60 degrees.

Here, we are once again making use of the Mosaic images of the M86 field from Rhode & Zepf (2004), but this time our goal is to search for evidence of substructure across the entire field. Because M86 was the primary target of the original study, it appears at the center of the Mosaic images, and M84 is positioned on the western edge (see Figure 4.1). At the distance of M86 ($\sim$17 Mpc), the $36'$ x $36'$ field-of-view of the Mosaic images corresponds to a physical area of roughly 180 kpc x 180 kpc. Besides M86 and M84, several other less luminous Virgo Cluster galaxies appear in the frames. The basic properties of the galaxies that appear in the Mosaic images are shown in Table 4.1 and drawn from the NASA/IPAC Extragalactic Database (NED), unless otherwise specified here or in the table note. The table lists: the galaxy name (i.e., the NGC number, along with the Messier catalog number and/or the VCC number); the morphological type from RC3 (de Vaucouleurs et al. 1991); the total absolute magnitude in the V-band (calculated by combining V_T^0 from RC3 with the distance modulus $m - M$ in table column (5)); an estimate of the stellar mass of the galaxy, computed by combining the V-band absolute magnitude with the appropriate mass-to-light ratio for spiral, S0, or elliptical galaxies, drawn from Zepf & Ashman (1993); the galaxy distance modulus and distance in Mpc; and the heliocentric radial velocity of the galaxy. The table also includes (when available) information about the total number of GCs in the system ($N_{\rm GC}$), the specific frequency S_N of the GC system (the number of GCs normalized by the V-band absolute magnitude of the galaxy, as defined by Harris & van den Bergh 1981), and T, the total number of clusters

normalized by the stellar mass of the galaxy (as defined by Zepf & Ashman 1993). As the information in Table 4.1 shows, nearly all of the galaxies that appear in our images have distances within the range ∼16 to 18 Mpc; one galaxy, NGC 4387, has a somewhat larger distance (21 Mpc) and another, IC 3303, has no redshift-independent distance measurement in NED. For the latter, we have assumed a distance modulus of 31.15 (17 Mpc) because the galaxy is included as a likely Virgo Cluster member in Binggeli et al. (1985).

Table 4.1. Properties of the Galaxies in the M86/M84 Images

Name	Type	$M_{\rm V}^{\rm T}$ (mag)	$\log_{10}(\mathrm{Mass}_*)$ ($\log(M_\odot)$)	$m-M$ (mag)	Distance (Mpc)	V_r (km s^{-1})	$N_{\rm GC}$	S_N	T
NGC 4374 (M84, VCC 0763)	E1	−22.3	11.8	31.32±0.11	18.4	1017±5	2800±200	3.5±0.5	4.1±0.6
NGC 4387 (VCC 0828)	E5	−19.6	10.8	31.65±0.73	21.4	565±5	41±9	0.6±0.3	0.6±0.3
NGC 4388 (VCC 0836)	Sb	−21.7	11.4	31.29±0.20	18.1	2524±1	70±10	0.3±0.1	0.6±0.3
NGC 4402 (VCC 0873)	Sb	−20.0	10.7	31.02±0.20	16.0	232±5	110±10	1.5±0.3	2.2±0.7
NGC 4406 (M86, VCC 0881)	E3	−22.3	11.9	31.17±0.14	17.1	−224±5	2900±400	3.5±0.5	4.1±0.6
NGC 4425 (VCC 0984)	SB0	−19.4	10.6	31.13±0.80	16.8	1908±5	90±10	1.6±0.5	2.5±0.8
NGC 4406B (VCC 0882)	dE3,N	−15.2	...	31.17±0.14	17.1	1101±55	...	...	...
IC 3303 (VCC 0781)	dS0,N	−17.5	...	...	...	−332±6	...	...	...

Notes. — For NGC 4402, no V-band magnitude is given in RC3 or in the NED listing. Therefore to calculate absolute V-band magnitude for this galaxy, we have combined B_T^0 from RC3 with an assumed $B-V$ color of 0.65, which is typical for Sb spiral galaxies (Roberts & Haynes (1994)), and the distance modulus in column (5). Distance modulus values for NGC 4374, NGC 4837, and NGC 4406 are from Tonry et al. (2001). Distance modulus values for NGC 4388 and NGC 4402 are from Tully et al. (2013) and the value for NGC 4425 is from Tully (1988). The morphological type for NGC 4406B is taken from Binggeli et al. (1985). There is no redshift-independent distance listed in NED for NGC4406B, so we assume the same distance as that of NGC 4406, because these two galaxies are thought to be interacting (Elmegreen et al. 2000). IC 3303 also has no redshift-independent distance measurement in NED, but because it is identified as a Virgo Cluster member, we have assumed a distance of 17 Mpc ($m-M=31.15$). For both NGC 4406B and IC 3303, we have taken B_T^0 from Binggeli et al. (1985) and combined it with the median $B-V$ value of 0.77 for early-type dwarf galaxies from van Zee et al. (2004) and the distance modulus to calculate the M_V^T value listed in column (3). The sources for the heliocentric radial velocities listed in column (6) are as follows: the values for M84, NGC 4387, M86, and NGC 4425 are from Cappellari et al. (2011); the value for NGC 4388 is from Lu et al. (1993); the value for NGC 4402 is from Binggeli et al. (1985); the velocity for NGC 4406B is from Strauss et al. (1992); and the velocity for IC 3303 is from Albaretti et al. (2017). The GC system properties are drawn from Young (2016) in all cases except NGC 4406, which are taken from Rhode & Zepf (2004), and NGC 4402, which are drawn from Rhode et al. (2022, in preparation).

For the analysis of M86 that was published in Rhode & Zepf (2004), the other galaxies and globular cluster populations in the Mosaic field were masked out so that the global properties of M86's globular cluster system (i.e., the total number of globular clusters, along with the specific frequency, radial distribution, color distribution, and color gradient of the system) could be quantified. For the current analysis, our aim was to look for substructure and environmental effects in the globular cluster populations in all the galaxies in the field, so we utilized the full Mosaic images without masking any large areas. To generate a list of globular cluster candidates across the full field, we carried out the same basic steps that had been used for the Rhode & Zepf (2004) analysis. We began by creating smoothed versions of the Mosaic images using a ring filter with a diameter equal to 6 times the FWHMPSF of the images. We then subtracted the smoothed images from the original images, thereby removing the diffuse starlight associated with the galaxies. A constant background level was added to the galaxy-subtracted images in order to restore the sky background before the source detection and photometry steps. Next we masked a small central portion of each galaxy (e.g., the central $\sim$200 x 200 pixels in M86 and M84) where the CCD image was saturated and/or where high noise levels in the galaxy-subtracted images prevented the detection of point-source globular cluster candidates. We then used IRAF DAOFIND to detect the sources in each image and we matched the source lists to produce a list of objects that appear in all three filters. We followed the same procedures that were described and illustrated in Rhode & Zepf (2004) to remove objects that appear extended in the Mosaic images: we measured the FWHM of the radial profile of each source and discarded objects that had larger-than-typical FWHM values for their instrumental magnitudes. At the distances of the Virgo Cluster galaxies in our field, globular clusters will be unresolved in our ground-based images, so objects with large measured FWHM are likely to be faint background galaxies rather than genuine globular clusters.

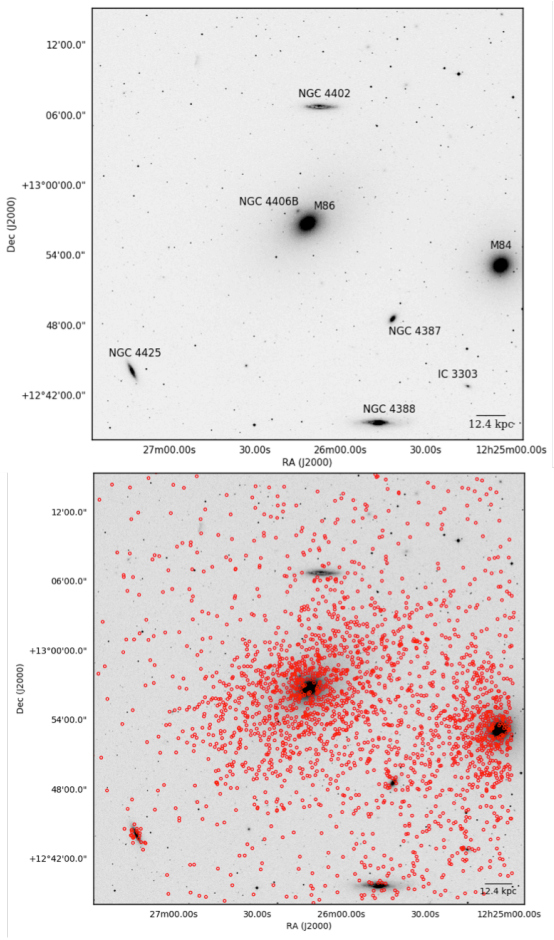

Figure 4.1 Upper Panel: A Digitized Sky Survey image showing the field-of-view of our Mosaic imaging data, with the eight galaxies in the field labeled. Our images span a 36′ x 36′ FOV and are centered on the giant elliptical galaxy M86 (NGC 4406). The properties of each of the galaxies in the field are given in Table 4.1. The 2.5′ scale bar corresponds to a length of 12.4 kpc (assuming a distance to the Virgo Cluster of 17 Mpc). Lower Panel: The same field with the spatial positions of the 2250 selected globular cluster candidates (marked as red circles, and selected as described in Section 4.1 and illustrated in Figure 4.2) in our sample.

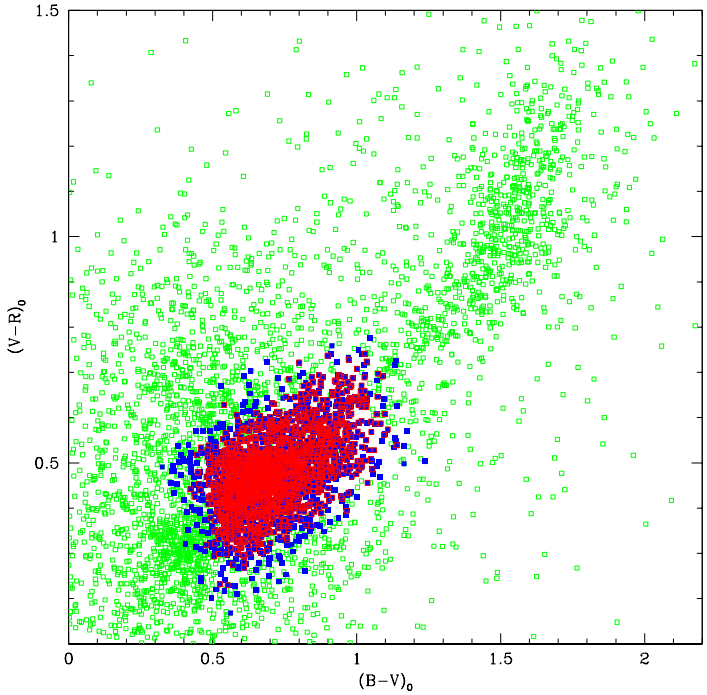

Figure 4.2 Color selection of globular cluster candidates in the M84/M86 field. The positions in the $V-R$ vs. $B-V$ color-color plane of 5921 point sources that appear in all three filters (B, V, and R) and survived the extended source cut step are plotted as green open squares. The 2250 globular cluster candidates, which are chosen because they have V magnitudes and $V-R$ vs. $B-V$ colors consistent with their being globular clusters at the distances of the target galaxies, are plotted as blue filled squares. The subset of 1718 globular cluster candidates that satisfy the criteria for the 90%-complete color sample are plotted on top of the latter, and are shown as red open squares. Details of the globular cluster candidate selection process are given in the text in Section 4.1.

Again following the same procedures as were used in the original analysis in Rhode & Zepf (2004), we performed aperture photometry on the sources that survived the extended source cut. We measured the light from each source within a small aperture (with a radius equal to the FWHMPSF value for a given image) and then applied the appropriate aperture correction and calibration coefficients to calculate calibrated V magnitudes and $B-V$ and $V-R$ for each source. The aperture corrections were calculated by measuring the magnitudes of a set of $\sim$20$-$40 bright stars in each image and computing the mean difference between the total magnitude and the magnitude within the small aperture. The aperture corrections (total magnitude minus magnitude within the small aperture) ranged from -0.15 to -0.21 mag with standard deviations of 0.01$-$0.02 mag. The Mosaic images of the M86+M84 field were acquired on a night with variable sky conditions, so we calibrated them using BVR exposures of the same field acquired under photometric conditions with the WIYN 3.5-m telescope[3] and Minimosaic camera. We measured magnitudes and colors for a set of bright stars that appeared in both sets of images and used these values to calculate a set of calibration coefficients (color transformation coefficients and zero-point constants) that could be applied to the Mosaic data.

We then used our final, photometrically-calibrated point-source photometry to select globular cluster candidates, i.e., unresolved objects with V magnitudes, $B-V$ colors, and $V-R$ colors that are consistent, within the photometric errors of each object, with the magnitudes and colors expected for globular clusters at the distances of the target galaxies. The BVR magnitude and color selection criteria were originally developed for the globular cluster system survey mentioned earlier in this section (Rhode & Zepf 2001, 2004). For the current analysis of the galaxies that appear in the M86/M84 field, we selected all point sources in the field with V magnitude

[3]The WIYN Observatory is currently operated as a joint facility of the NSF's National Optical-Infrared Astronomy Research Laboratory, Indiana University, the University of Wisconsin-Madison, Pennsylvania State University, the University of California-Irvine and Purdue University.

greater than 20.0 and colors within a specific region of the $V-R$ vs. $B-V$ color-color relation defined by Milky Way globular clusters (Rhode & Zepf 2001). The V magnitude criterion is based on the assumption that the brightest globular cluster in the target galaxies will have $M_V \sim -11$ mag. We note that the galaxies in the M86/M84 field have a range of distance moduli (from 31.02 to 31.65), so $M_V = -11$ corresponds to a slightly different apparent V magnitude for each galaxy. However, because the $B-V$ and $V-R$ color also play a role in the selection, the final list of globular cluster candidates remains the same whether we apply the $V > 20.0$ magnitude criterion across the entire field, or apply a slightly different V threshold for objects around each galaxy that takes into account the varying distance moduli of the galaxies. The $B-V$ and $V-R$ color criteria are explained in detail in Rhode & Zepf (2001); briefly, we select objects that have $B-V$ values between 0.56 and 0.99 (which is the $B-V$ range expected for globular clusters with [Fe/H] between 0.0 and -2.5, based on the observed colors of Galactic globular clusters) and $V-R$ values that put them within 3 times the standard deviation of the $V-R$ vs. $B-V$ relation for Milky Way globular clusters. The selection process yielded a final list of 2250 globular cluster candidates across the entire M86/M84 field. Figure 4.2 shows the globular cluster candidates (blue filled symbols) in the $V-R$ vs. $B-V$ color-color plane, along with the other unresolved sources in the field that were not selected (green open symbols). Note that because the photometric errors for each object are taken into account in the GC candidate selection, the selected candidates (the blue symbols in Figure 4.2) extend over a slightly larger region of the color-color plane than they would if the errors were not considered. The spatial locations of the GC candidates in the M86/M84 images are shown in the bottom panel of Figure 4.1.

Removing extended objects from the source lists and then selecting globular clusters based on their magnitudes and colors in three filters significantly reduces the contamination in our sample (e.g., Rhode & Zepf 2001, 2004), although some con-

tamination inevitably remains. Our analysis has shown that many of the contaminating objects that coincide with the globular cluster selection box in the $V-R$ vs. $B-V$ plane are compact background galaxies that are faint enough that they cannot be distinguished from point sources, and some are foreground Galactic stars (Rhode & Zepf 2001, 2004; Hargis & Rhode 2012).

To assess the amount of contamination in the globular cluster candidate sample and then correct for it in subsequent steps, we created radial surface density profiles for the globular cluster systems of M84 and M86. We assigned the globular cluster candidates around each galaxy to a set of $1'$-wide annuli, based on the candidates' projected radial distances from the galaxy center. We calculated the area of the portion of each annulus where globular clusters could be detected, i.e., the area minus those parts of the annulus that were masked out (because, for example, they included bright foreground stars or areas with cosmetic defects on the CCD) or extended off the edges of the images. We then computed the surface density (number per unit area on the sky) of globular cluster candidates for each annulus to construct the radial surface density profile of the system. The surface density values were highest near the center of each galaxy and then tapered off to a constant, flat value in the outer regions. We calculated the weighted mean of the surface density in the outer few annuli, where the surface density was constant, and used this as an estimate of the contamination level in the globular cluster candidate sample. We carried out this analysis for M84 and M86 independently (masking a large region around the neighboring galaxy, and then carrying out the steps to construct the radial profile of the unmasked galaxy), and found that these estimated contamination levels matched each other within the uncertainties. We also checked to make sure that the contamination correction was the same on the east and west sides of M86, and on the north and south sides of M84. The estimated contamination level in the globular cluster candidate list for the M84/M86 field is 0.2997+/-0.0268 per sq. arcmin. Given the area of the images

(1378 square arcminutes), this works out to approximately 413 objects over the entire field, out of the 2,250 objects in the GC candidate list.

Because we select globular cluster candidates via their V magnitudes and $B-V$ and $V-R$ colors, any contaminants that are present in the globular cluster candidate list will have similar magnitudes and colors as the true globular clusters in the sample. Nevertheless we decided to apply a statistical correction to account for contamination in the globular cluster candidate sample before carrying out our search for spatial features and substructure in the M86/M84 field. Details about the contamination corrections applied for each part of the analysis are given in Section 4.2.

We carried out a series of artificial star tests in order to quantify the detection limits for point sources in each of the Mosaic images and determine how much of the Globular Cluster Luminosity Function (GCLF) we are able to detect in the target galaxies. We carried out these tests on the B, V, and R images separately. For each test, we added artificial point sources to a given image, executed the same set of steps we had used to detect the globular cluster candidates, and then determined how many of the artificial sources were recovered. We added 800 artificial objects to each image, in steps of 0.2 magnitude, and repeated the process until we had covered a magnitude range of 5-6 magnitudes in each filter. The results of the artificial star tests show that our detection process is 50% complete for point sources with B =25.0, V =24.0, and R =23.4. We can combine the results of the completeness testing in each of the three filters in order to estimate how much of the intrinsic GCLF we have detected. Given our point-source detection limits in B, V, and R, and the requirement that cluster candidates are detected in all three filters, and assuming an intrinsic GCLF with a peak magnitude ($M_V \sim -7.4$ mag) and dispersion ($\sigma \sim 1.4$ mag) (Brodie & Strader 2006, and references therein) we estimate that we have detected approximately 50% of the intrinsic GCLF (i.e., the brightest 50% of the clusters within the field-of-view of our images) of the two massive ellipticals M84 and M86.

The numbers above show that the detection completeness varies in each filter – the B image is substantially deeper than the R image. In addition to producing the full list of all 2250 globular cluster candidates in our images, we also wanted to produce a list that we could use to explore how certain features in the spatial distribution of clusters vary when we examine subpopulations of clusters selected by their colors (see Section 4.2.2). In other words, we need to construct a sample of globular clusters that is equally complete in all three filters, to be sure that no color selection bias is present in the subsample being used to investigate trends with globular cluster color. To accomplish this, we defined a sample of objects that we refer to as the "90% color sample", because it is at least 90% complete in all three filters. The reddest globular cluster candidate in the full list of 2250 clusters has $B - R = 1.87$, and in the B-band our detection is 90% complete at 24.77, so a 90%-complete color sample would include all GC candidates with R brighter than 22.9. Applying this criterion to our GC candidate list yields a sample of 1718 objects. The locations of these 1718 objects in the $V - R$ vs. $B - V$ color-color plane are shown in Figure 4.2, plotted in red open symbols on top of the 2250 globular cluster candidates in the full sample.

In the globular cluster system color distributions of elliptical galaxies, the blue, metal-poor peak often occurs around $B - R \sim 1.1$, the gap between the two populations is typically around $B - R = 1.23$, and the second peak appears at $B - R \sim 1.4$ (e.g. Rhode & Zepf 2001, 2004). Therefore to investigate how the substructures in the M86/M84 field might vary for the different globular cluster subpopulations, we divide our 90% color sample into two subsamples at $B - R = 1.23$. We use these blue and red subsamples in the analysis presented in Section 4.2.2. We also explain in that section how we used the estimated contamination level (discussed earlier) to apply a statistical correction for contamination to these subsamples.

4.2 Analysis and Results

We began our analysis by creating surface density maps of the globular cluster candidates in the M84/M86 field. To look for evidence of substructure, we divided the field into a 150 x 150 grid and used Kernel Density Estimation (e.g. Silverman 1986; Ivezić et al. 2014 for a detailed description of the technique) to calculate the surface density maps. Iso-density contours were then added to each map to help emphasize surface density features within the field. We used a Gaussian kernel with a fixed bandwidth of $0.86'$ (corresponding to $\sim$200 pixels). This bandwidth was chosen because it appeared to strike the best balance between smoothing away noise within the data while still allowing large-scale substructure to emerge.

4.2.1 M86 Surface Density Map

Figure 4.3 shows the surface density map for the full GC candidate sample. As explained in the previous section, some of the objects in the sample will not be true globular clusters but will instead be compact objects (foreground stars and background galaxies) that have magnitudes and colors like globular clusters at the distances of the target galaxies, and our sample of 2250 GC candidates should contain approximately 413 of such contaminating objects. To correct for contamination, we artificially cleaned the data by randomly selecting and removing 413 objects from the list of 2250 GC candidates. We then performed the KDE analysis on the cleaned data set. We carried out these steps a total of 100 times, removing a different random set of 413 objects each time. From the 100 realizations, we calculated the average surface density for each cell and used those averaged values to create the final KDE map shown in Figure 4.3. We find three major features, marked with an A, B, or C in the figure, along with three minor features. We discuss each of these features below.

There are several minor features of note in the surface density map. First, there

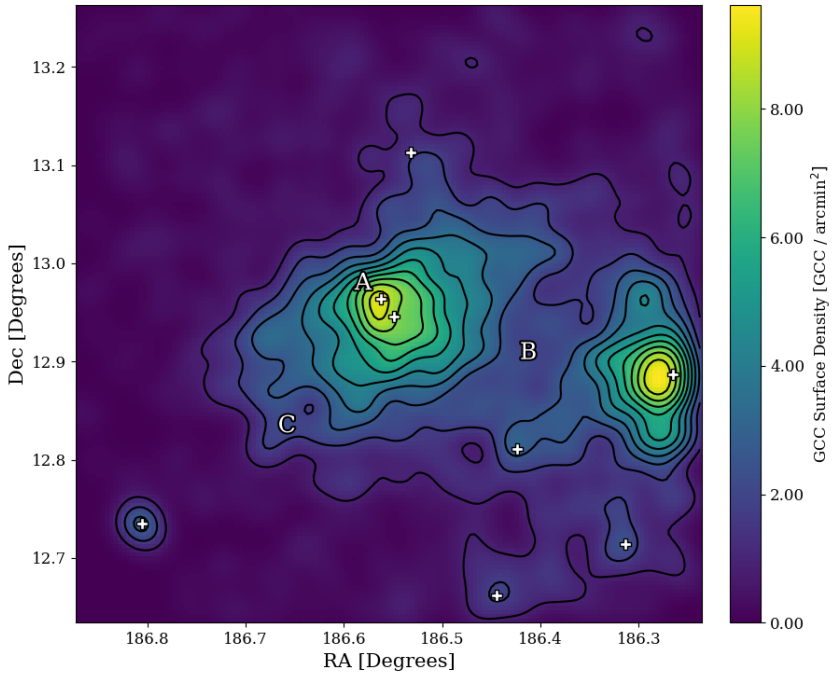

Figure 4.3 The GC candidate surface density map of the M86 field with contours overlaid. The data were artificially cleaned by randomly selecting and removing the expected number of contaminants from the globular cluster candidate list and performing a KDE analysis on the objects that remained. This was done 100 times with the average density in each grid cell calculated and used to create the final image. The most apparent features are an offset peak in the M86 GC system (A), a bridge connecting M86 to NGC 4387 and M84 (B), and a flattening of the iso-density contours along the southeast side of the M86 GC system (C). The figure is oriented such that north is up and east is to the left and white crosses indicate the positions of galaxies within the field

.

appears to be a surface density peak in the M84 GC system located $\sim 1'$ to the east of the center of M84. It is important to note that this is an artifact of our method rather than a true surface density anomaly. This offset is a product of edge effects caused by M84's position near the edge of our field. Due to the nature of the KDE technique, surface densities near the edge of the field will be systematically underestimated because we cannot account for GCs that are present, but fall outside our field of view. We varied the kernel size and found the position of this surface density peak largely depended on this parameter, with smaller kernel sizes causing the peak to migrate to the west, toward the center of M84. However, decreasing the kernel size to the degree needed to remove the offset of the surface density peak greatly increased the prominence of noise within the image.

There is also a small connection between the GC systems of M86 and NGC 4402 that appears to indicate a tidal interaction. We used the results from our analysis of NGC 4402's GC system (see Table 4.1; Rhode et al. 2022, in preparation) to help us investigate whether this connection might be genuine evidence of a tidal interaction or simply the result of the two GC systems overlapping in projection on the sky. We removed the globular cluster candidates around NGC 4402 within $2'$ (one $R_{\rm eff}$ for the globular cluster system) of the galaxy center; there were 23 candidates inside $2'$ in the full sample, and 13 blue candidates and five red candidates in the 90% color sample. We then repeated the KDE surface density map analysis but with those objects removed. Even with the removal of the GC candidates associated with NGC 4402, the connection still appears in all of the KDE surface density maps, although at a reduced strength.

Lastly, in the southeast corner of the field lies NGC 4425, an SB0 galaxy with a remarkably symmetric GC system. While the galaxy is relatively modest in size and mass (with a total magnitude of $M_V^T = -19.4$ and an estimated population of 90 ± 10 globular clusters; see Table 4.1), it is interesting that it has survived within the Virgo

Cluster without, on first inspection, having had any significant tidal interactions to distort its GC system.

4.2.1.1 A Spatial Offset in the Peak Surface Density of the M86 Globular Cluster System

Feature A in Figure 4.3 is a peak in the GC system surface density that is approximately $0.7'$ away from the center of M86. This surface density peak is similar to an over-density reported by D'Abrusco et al. (2015) that lies in roughly the same area. In addition to the unexpected position of the surface density peak, there is a distortion in the central region of the M86 GC system where the surface density contours are elongated along the northeast to southwest direction.

Since the masked portion of the galaxy (the central $\sim$200 x 200 pixels, which are masked because they are saturated in the CCD images) is close to this surface density peak, we first attempted to determine if this offset might be due to the same kinds of edge effects that created the offset in the M84 surface density peak. Decreasing the kernel size did not cause the peak to migrate towards the center of M86, so we created a $1'$ wide annulus just outside and surrounding the masked region and calculated the surface density within this annulus. We then used this surface density along with the area of the masked region to determine the expected number of GC candidates that are likely to be inside the masked region and thus undetected in the images. We randomly distributed the same number of artificial GC candidates within the masked region and used KDE to create a new surface density map. The lopsided morphology of the innermost region of the M86 GC system seen in the original KDE map is still present in this new map.

To quantify the significance of this offset peak, we compared this finding to the expected case of an unperturbed, azimuthally-symmetric GC system. To do this, we first needed to know the parameters that describe the M86 GC system. As mentioned

in Section 4.1, Hargis & Rhode (2014) used the Mosaic images from which our sample was derived to study the spatial distribution of the GC system of M86. They found that the morphology of the inner region of the M86 GC system can be characterized by an ellipse with a semi-major axis length of 9.2′, an ellipticity of 0.38, and a position angle of -63° east of north. We created an ellipse with these same characteristics and then divided it into 6 equal-area wedges with the center of the ellipse positioned to coincide with the center of M86. In an unperturbed GC system, we would expect each wedge to contain approximately the same number of GC candidates, but as can be seen in Figure 4.4, this is not the case. The left panel in Figure 4.4 shows our ellipse with the GC candidates and KDE contours plotted; the wedges are numbered and we plot the number of GC candidates in each wedge in the right panel. The horizontal blue line is the expected number of GC candidates in each wedge and the blue-shaded region marks the $\pm 1\sigma$ Poisson error on that number. The northeast wedge, number 6, has an excess of 20 GC candidates, $\sim 2.5\sigma$ higher than the expected number, suggesting that this offset GC candidate surface density peak is modestly significant.

It is notable that the dwarf galaxy NGC 4406B (VCC 882) coincides with this over-density. To estimate the number of GCs NGC 4406B might be contributing, we used the data gathered from a survey of dwarf elliptical galaxies by Miller & Lotz (2007). This survey included 13 nucleated dwarf ellipticals with absolute magnitudes between M_v = -15 and M_v = -16. The estimated number of GCs hosted by these 13 dwarf galaxies ranged from $\sim 2-22$ clusters. Considering this, it is reasonable to assume that NGC 4406B contributes, at least in part, to the over-density seen in Feature A. We compared the color distribution of GC candidates within this over-density to that of the GC candidates in the surrounding area. If NGC 4406B is contributing a significant number of clusters to this over-density, we might expect the color distribution of the GC candidates within the over-density to be shifted towards

slightly bluer colors compared to the GC candidates in the surrounding area. For example, Peng et al. (2006) found that lower-luminosity galaxies have GC systems with bluer mean colors compared to higher-luminosity galaxies, although with plenty of scatter in the relation (see Figure 3 in their paper).

We found 40 GC candidates within $0.9'$ of the over-density and compared their B-R colors to those of the GC candidates in the surrounding regions. We found no evidence to suggest that the GC candidates within this over-density tend to be bluer than the candidates in the surrounding regions, but with such a small sample size and small expected differences in the color distribution this excess is likely to be difficult to detect. It is also possible that this over-density is a result of interactions among the local GCs. Elmegreen et al. (2000) found that NGC 4406B is undergoing tidal stripping from M86, so a perturbation in the M86 GC system caused by NGC 4406B would potentially explain the existence of this over-density.

4.2.1.2 A High Surface Density Bridge Between M86 and M84

To the southwest of M86, in the area labeled with a B in Figure 4.3, an overdense region characterized by the presence of a few structural anomalies connects the GC systems of M86 and M84. This region incorporates the GC candidates associated with the moderate-luminosity elliptical galaxy NGC 4387, which has a contour around it that directly connects it to M84. Removal of the GC candidates associated with NGC 4387 does not noticeably affect the appearance of this bridge. The region labeled with a B contains several complex features – such as the overdense tail emerging to the east of M84 and the general lopsided morphology on the southwest side of M86 – that are not consistent with the expected spatial distributions of the M86 and M84 GC systems, but instead may be due to an interaction between the two populations.

This region also shares qualitative similarities to structures formed in simulations of galaxy interactions in clusters of galaxies (Rudick et al. 2011; Ramos-Almendares

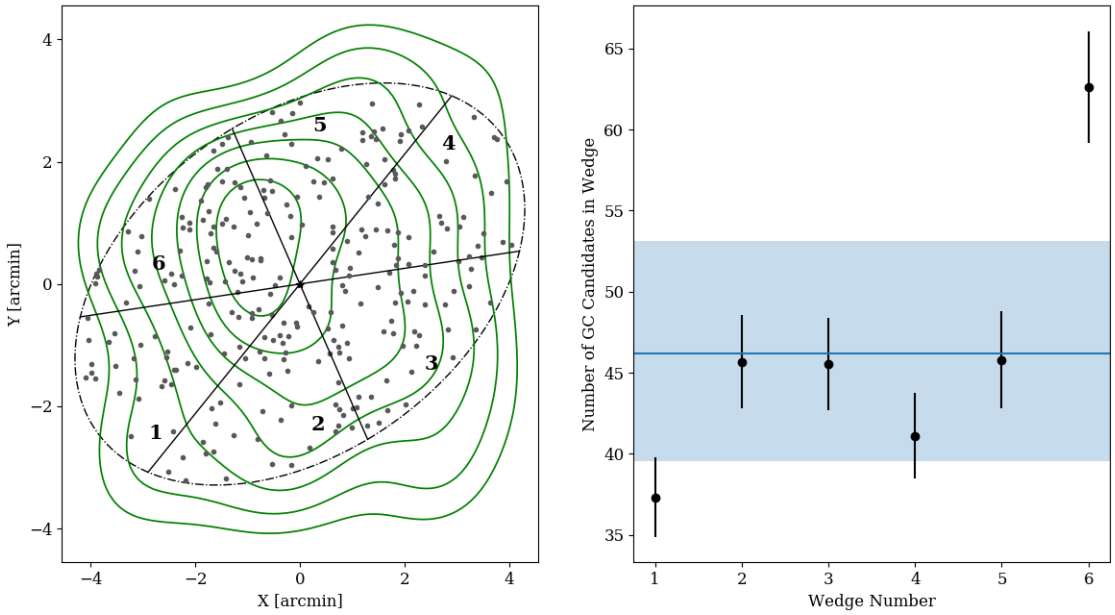

Figure 4.4 Left panel: The inner 9.2′ x 9.2′ of the M86 GC system. The dotted ellipse outlines the expected morphology of the M86 GC system using characteristics reported in Hargis & Rhode (2014) (semi-major axis of 9.2′, ellipticity of 0.38, position angle of -63° east of north). The ellipse is split into 6 equal-area, wedge bins and the green lines are contours generated from the KDE measured surface density of the GC candidates within the ellipse. From the contours, it can be seen that the main over-density in the M86 GC system is offset from the center. Wedges are numbered from 1 to 6 for ease of description. Right Panel: The number of GC candidates within each wedge plotted vs. the wedge number. The black points are the number of GC candidates in a given wedge, the blue line is the expected number of GC candidates in each wedge, given no azimuthal asymmetries, and the blue shaded region denotes the area within $\pm 1\sigma$ Poisson error of the expected number of GC candidates in each wedge.

et al. 2018), supporting the possibility that it is the result of an interaction between M86 and M84.

We considered the possibility that this bridge is a projection effect and created two KDE density maps for symmetric models of the M84 and M86 GC systems. For the M84-M86 GC systems the task of identifying symmetric equilibrium models reliably extending to the outer regions is complicated by the proximity of the two systems and the possible distortions caused by the interaction between them. For this reason, our equilibrium models for the two GC systems are based on the structural properties of the inner regions of the systems, and are unlikely to be perfect representations of the distributions of the GCs over the full radial range. Nevertheless, this is the best we can do given the location of the galaxies in the field and the limitations of the data set. We have modeled the two GC systems as follows: for M86, we use the parameters measured for the GC system by Hargis & Rhode (2014) with an ellipticity of 0.38, position angle of $-62°$, effective radius of 5.8 arcminutes, Sersic index of 0.9, and system extent of 17 arcminutes. The effective radius and Sersic index were obtained from the Sersic fit in Hargis & Rhode (2014) and chosen because these parameters appeared to better minimize residuals in this galaxy's GC system. For M84, we do not have measured quantities (the spatial coverage of the M84 data was insufficient for it to be modeled by Hargis & Rhode 2014) so instead we adopt an ellipticity of 0.1, position angle of 0 degrees, Reff of 6.6 arcminutes, Sersic index of 2.4, and system extent of 15.4 arcminutes. The ellipticity was estimated based on the galaxy morphology. The Sersic index was determined by radially fitting the distribution of GC candidates into 1 arcminute wide annuli within 10 arcminutes of the M84 GC system center.

We then created a residual density map by subtracting the average density map (based on 100 realizations) of these two symmetric models from the KDE map obtained from observational data. The residual density map showed several over-

densities associated with features that could not be explained by a simple overlap of the two GC systems. Specifically, the strong lopsidedness of the M86 GC system (the southwest region of the M86 GC system adjacent to the bridge), the SE shelf (marked by the letter C), and the elongated stream of GCs emerging from M84 creating a bridge between M84 and M86 (marked by the letter B) are likely to be a consequence of the interaction between the GC systems of these two galaxies or, in the case of the SE shelf, of major accretion event in the galaxy's past (as suggested by Mihos et al. 2017).

4.2.1.3 Flattened Contours on the Southeast Side of M86

The area of the GC system along the southeast edge of M86, labeled with a C in Figure 4.3, has flattened iso-density contours. This flattening breaks from the expected elliptical shape of the M86 GC system morphology (see Section 4.1). There is not a similar flattening in the contours along the northwest edge of the M86 GC system. This gives an "egg-like" shape to the iso-density contours on the southeast side of M86 and suggests that an accretion event or tidal interaction may have occurred that redistributed the GCs in that region.

We compared the locations of the features we found in the GC populations to results from two studies that searched for low-surface brightness substructures in this area of the Virgo Cluster. Janowiecki et al. (2010) used V-band surface photometry to probe the halos of the five brightest ellipticals in the Virgo Cluster for diffuse light features. To observe features nearer the galaxy center, they fitted elliptical isophotes to the galaxy light and subtracted them, leaving behind the diffuse light features. Mihos et al. (2017) searched the intracluster light between and around galaxies within the Virgo Cluster to detect low-surface brightness features that could indicate past interactions or hierarchical processes. To achieve the depth required to observe features formed from the intracluster light, Mihos et al. (2017) stacked their

images and then removed contamination from Galactic cirrus. Figure 4.5 shows our surface density map with the yellow regions marking features detected in Janowiecki et al. (2010). From this figure we can see that the diffuse light structures reported by Janowiecki et al. (2010) have little to no obvious correlation with the features in our GC candidate surface density map. The region directly to the north of M84 appears to coincide with a small over-density in the surface density map, but because of the proximity to the edge of our field, it is possible that this over-density in the GC system is a spurious result due to edge effects. On the other hand, there is a similarity between our detected features and a feature that was found in the Mihos et al. (2017) study of the M86/M84 field. Mihos et al. (2017) detected an extended low surface brightness feature along the southeast (SE) edge of the M86 halo that did not match the elliptical isophotes and may, they suggested, be a consequence of a major merger event. This substructure is in the same direction as feature C and both are characterized by boxier contours, although the feature we find is comparatively closer in to the galaxy center whereas the "SE Shelf" identified by Mihos et al. (2017) is formed from diffuse light in the outermost regions of the galaxy.

4.2.2 Surface Density Maps of the Red and Blue GC Candidates

Figure 4.6 shows the surface density maps of the subsamples of GC candidates that are classified as either blue (metal-poor) or red (metal-rich) according to the criteria described in Section 4.1. To construct this sample and correct it for contamination, we began with the full list of 2250 GC candidates. We randomly removed 413 objects from the sample, and then applied the appropriate R magnitude cut (selecting GC candidates brighter than $R = 22.9$; see Section 4.1) to produce a contamination-corrected 90% color sample. We then divided the contamination-corrected sample into blue and red subsamples at $B - R = 1.23$. As we had done when we constructed the main KDE map shown in Figure 4.3, we repeated these steps (randomly removing

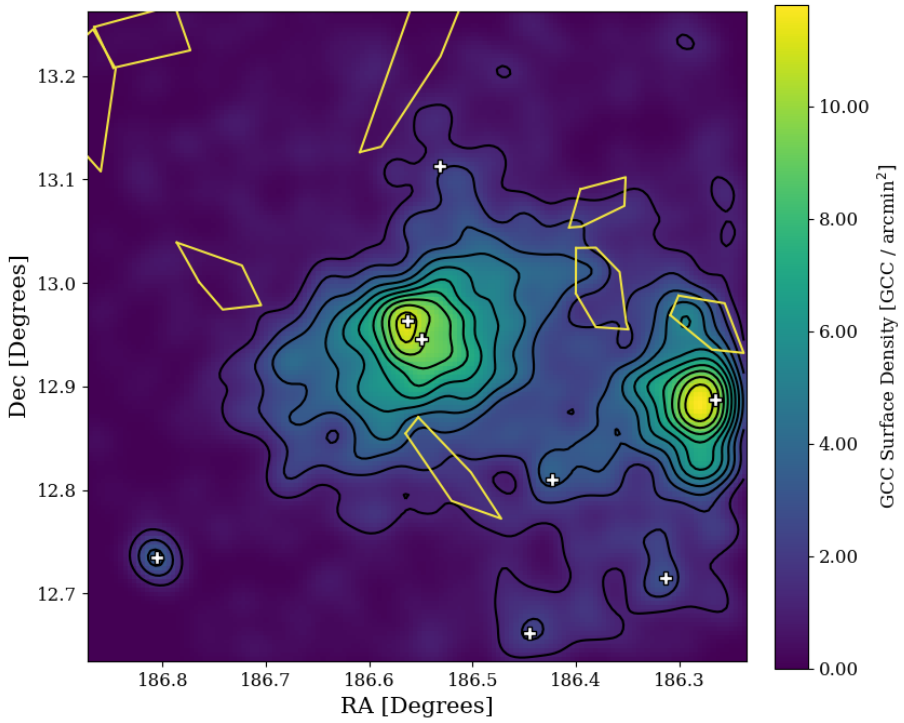

Figure 4.5 A comparison of our GC candidate surface density map to the regions outlining diffuse light features reported by Janowiecki et al. (2010). The yellow boxes correspond to regions surrounding low-surface brightness features. In general, there appears to be little correlation between the substructures seen in the GC candidate surface density and those found using diffuse light in Janowiecki et al. (2010). Galaxy positions in the field are marked with white crosses.

GC candidates to account for contamination, and then applying completeness cuts and splitting the samples according to color) 100 times, removing a different selection of GC candidates each time. In each realization, the surface density was estimated at each cell in our grid and the average surface density for each grid cell was calculated from this collection of estimates.

The blue GC candidates, shown in the upper panel of Figure 4.6, have a more extended spatial distribution compared to their red counterparts. In the surface density map of the blue GC candidates, we see a recurrence of the surface density peak to the northeast of the M86 GC system center that was visible in the map of the full GC candidate sample (feature A from Figure 4.3). The contours in the inner region of the blue component of the M86 GC system are increasingly elongated along the northeast-southwest axis, suggesting that this elongation comes primarily from the blue GC candidates in the sample. Likewise, the bridge connecting the M86 and M84 GC systems (feature B from Figure 4.3) is prominent, with a high surface density arm connecting M84 to NGC 4397 and another high surface density arm emerging from the M86 GC system along the southwest direction. The southeast shelf is still present, but has broken down into patchier, high surface density regions. Furthermore, many of the less luminous galaxies in the field have high-density regions associated with them in the blue GC candidate KDE map, but these high-density regions are much weaker, if they exist at all, in the red GC candidate KDE map. This is not unexpected, because lower-luminosity galaxies tend to have smaller proportions of metal-rich GCs than more luminous galaxies do (e.g., Peng et al. 2006).

In contrast to the blue GC candidates, the red GC candidates (lower panel of Figure 4.6) are more centrally concentrated. The bridge linking the M86 and M84 GC systems is much weaker, but still present, with a connection formed just north of NGC 4387. The asymmetric surface density peak to the northeast of the M86 GC system center has almost entirely disappeared. The surface density contours in

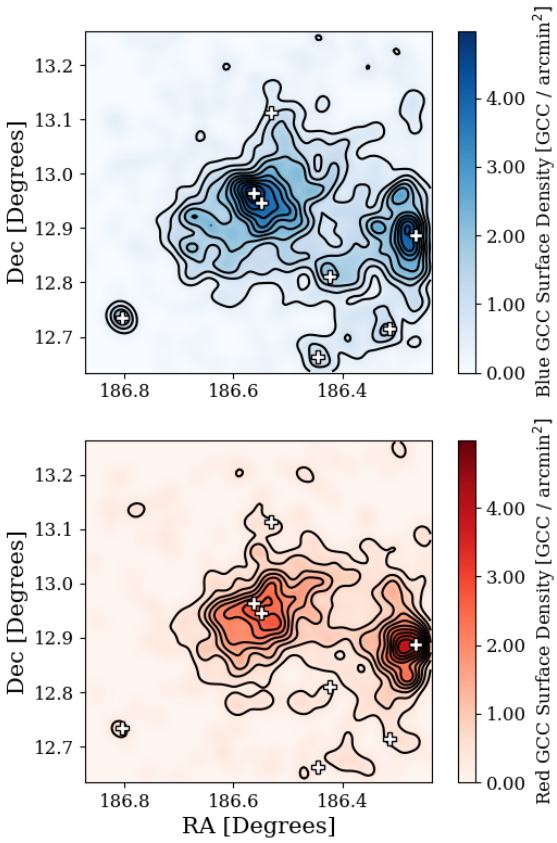

Figure 4.6 Top Panel: The KDE surface density map of the blue GC candidates in our sample. The high surface density bridge between M86 and M84 has been divided into two bridges, one connecting NGC 4387 to the M84 GC system and one stretching southwest from M86 towards NGC 4387. Bottom Panel: The KDE surface density map of the red GC candidates in our sample. The red GC candidates are more centrally condensed. A small, high-surface density bridge connects the M86 GC system to the M84 GC system, with another connection almost forming to the north of both systems. The asymmetry in the central region of the M86 GC system has disappeared, with the highest surface densities occurring in the middle of the GC system. Both figures are oriented such that north is up and east is to the left. In both panels, galaxy positions are marked with white crosses.

the central region of the red component of the M86 GC system also do not show the same distortion along the northeast-southwest direction that is seen in the blue component, reinforcing that these two features are dominated by metal-poor globular clusters. The southeast shelf is largely non-existent in the surface density map of the red GC candidates. Instead, the central region of the red component of the M86 GC system has boxier iso-density contours than those in the blue GC candidate surface density maps.

4.2.3 Spatial Positions of GCs with Velocities

Having kinematic data for some of the GC candidates in our sample should provide us with additional insight into the accretion history and ongoing interactions between the GC populations in this well-populated Virgo Cluster field. To further investigate the possibility of substructure in the GC populations of the galaxies, we explored kinematic data published by Park et al. (2012) and Ko et al. (2017). Park et al. (2012) measured the radial velocities of 25 GCs around M86 and reported a mean GC velocity of $v_p = -354^{+81}_{-79}$ km s^{-1} with a velocity dispersion of $\sigma_p = 292 \pm 32$ km s^{-1}. Ko et al. (2017) carried out a wide-field spectroscopic survey of GCs within the Virgo Cluster. Of the 201 GC spectra in the Ko et al. (2017) sample, 94 GCs were within our field, with one of these GCs also appearing in the Park et al. (2012) sample. After combining the Park et al. (2012) and Ko et al. (2017) data sets and removing the one duplicate GC, we had a total of 118 GCs with radial velocities in our field to study.

Figure 4.7 shows a map of the spatial distributions of the collated sample of GCs within our field from the Park et al. (2012) and Ko et al. (2017) surveys plotted on top of the surface density map of our full, contamination-corrected GC candidate sample. The points representing the GCs are color-coded according to their radial velocity in km s^{-1} and the spatial positions of galaxies within the field are denoted

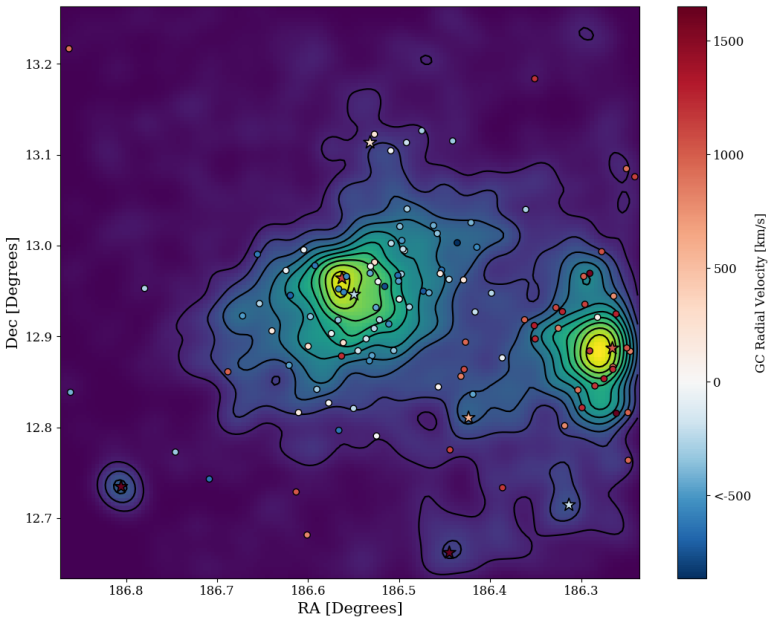

Figure 4.7 The spatial distribution of GCs with measured radial velocities in the region around M86 (left) and M84 (right). The GCs are plotted on top of the contamination-corrected KDE map of our full GC candidate sample. Each GC with a measured velocity is color-coded according to its reported radial velocity, with red GCs receding and blue GCs approaching. Each galaxy's position is marked with a star with the color indicating that galaxy's radial velocity.

by stars, also color-coded according to their radial velocities as reported in Table 4.1. From this figure it can be seen that GCs with measured velocities populate all of the major features discussed previously. The GC candidate surface density peak to the northeast of M86's spatial position has three clusters with negative radial velocities, consistent with the velocity of M86 (-224±5 km s^{-1}). The bridge of elevated GC candidate surface density that connects the M86 and M84 GC systems is populated by several GCs with varying radial velocities, suggesting it is comprised of GCs from both galaxies and, possibly, intracluster GCs. The flattened shelf along the southeast side of the M86 GC system is mostly populated by GCs with velocities consistent with the radial velocity of M86, but there are two GCs with high recession velocities more akin to the radial velocities of M84 (1017±5 km s^{-1}) or NGC 4406B (1101±55 km s^{-1}).

Most of the less massive galaxies in the field appear to host no, or very few, of the globular clusters with measured velocities. The barred lenticular galaxy NGC 4425 and the spiral galaxy NGC 4388 each have two clusters in close proximity with recession velocities similar to those of the galaxies, suggesting that the clusters are associated. NGC 4402 also has two clusters with similar velocities nearby, but its close proximity to M86 makes it difficult to assess to which galaxy's GC system these clusters belong.

We plot the radial velocity of these globular clusters as a function of their projected radial distance from the center of M86 in Figure 4.8. The clusters have been color-coded based on their proximity to either M86 or M84, with green points representing clusters with a smaller projected radial distance to the center of M86 and orange points representing clusters with a smaller distance to the center of M84. The radial velocities of M86 and M84 (as reported by Cappellari et al. 2011) are represented as the green and orange dashed lines, respectively, with the vertical, black dashed line denoting the projected radial distance between M86 and M84. There is clearly a

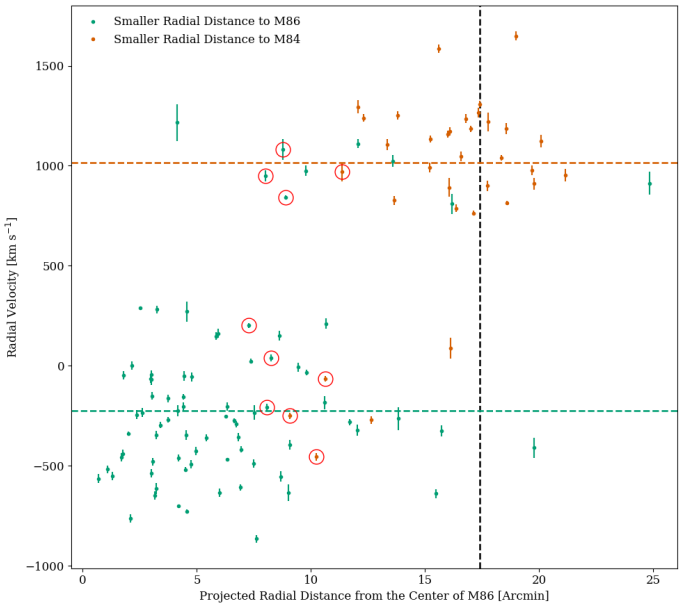

Figure 4.8 The radial velocities of GCs from the collated survey data of Park et al. (2012) and Ko et al. (2017) as a function of each object's projected radial distance from the center of M86. Points have been color-coded based on the closest massive elliptical galaxy, with green (orange) points having a smaller projected radial distance from M86 (M84). The three dashed lines are color-coded as follows: green represents the radial velocity of M86, orange represents the radial velocity of M84, and black represents the projected radial distance from the center of M84 to the center of M86. All data points have uncertainties associated with their measured velocities, but many of these uncertainties are smaller than the markers. The ten GC candidates located within the bridge between M86 and M84 are circled.

large gap between ∼300 km s^{-1} and ∼800 km s^{-1} where GCs are lacking; the large kinematic separation could be indicative of a fly-by interaction between M86 and M84. This plot also confirms the existence of several clusters with kinematics that are not consistent with the expected velocity based on their closest massive elliptical neighbor.

We attempted to quantify the significance of differences between the radial velocities of 114 GCs in this sample with the radial velocities of each GC's closest massive elliptical galaxy. We removed both sets of clusters nearest NGC 4425 and NGC 4388, as these GCs have radial velocities in close agreement with those of NGC 4425 and NGC 4388, and are unlikely to be hosted by either M86 or M84. To determine whether a GC had a radial velocity that was significantly different than the mean velocity of the nearest massive elliptical galaxy, we needed to estimate the velocity dispersion of the M86 and M84 GC systems. We did this using the biweight method described in Beers et al. (1990) with GCs within one effective radius of M86 and GCs within one effective radius of M84. We limited ourselves to GCs within one effective radius of each galaxy because of the significant overlap between the two systems. With this method we report a velocity dispersion of $\sigma_{v,M86} = 308^{+60}_{-49}$ km s^{-1} and $\sigma_{v,M84} = 265^{+83}_{-62}$ km s^{-1} calculated from 46 and 25 GCs, respectively.

In Figure 4.9, we color-code each GC based on the difference between the cluster's velocity and the average velocity of the closest massive elliptical galaxy (normalized to the velocity dispersion of the closest massive elliptical galaxy). The bridge connecting the GC systems of M86 and M84 hosts ten GCs. The GCs within this connection form a rough line from the northwest to the southeast, across the feature itself. These GCs have a range of velocities, from -454 km s^{-1} to +1081 km s^{-1}, and all of them have velocities consistent with those expected for GCs associated with either M86 or M84. However, as shown in Figure 4.9, six of these GCs have radial velocities that are 3σ to 6σ different from the radial velocity of their closest massive elliptical

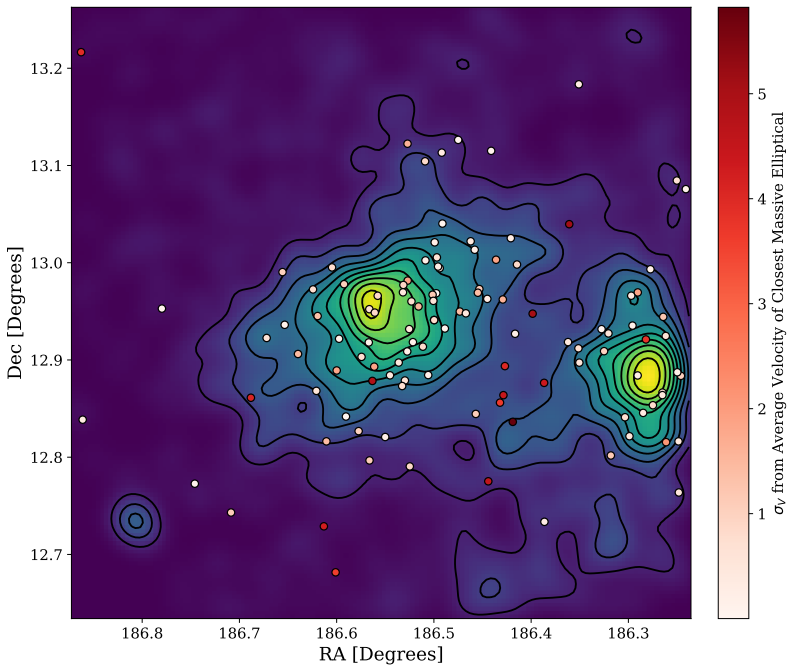

Figure 4.9 The spatial positions of the GCs with reported velocities, color-coded based on the difference between the GC velocity and the average velocity of the nearest massive elliptical galaxy. Most of the GCs with radial velocities inconsistent with their closest massive elliptical galaxy are located within the bridge and stretch along the east-west axis and to the south of the M86 GC system.

neighbor. Several of the clusters in the field surrounding the two galaxies, along with two clusters located between NGC 4425 and NGC 4388, have velocities consistent with the GCs of M84. Similarly, there are a few clusters that are located closer to the center of M84 but have velocities consistent with that of M86. Although some of the clusters in question may have been stripped by tidal interactions between the two massive ellipticals, they may also simply represent clusters in the outer regions of the globular cluster systems of M84 and M86. A significantly larger sample of velocities would be needed to construct a complete characterization of the phase space of these globular cluster systems, to explore the possible fingerprints of the tidal interaction between M84 and M86, and to identify a population of intracluster globular clusters (see, e.g., Romanowsky et al. 2012; Longobardi et al. 2015, 2018).

4.3 Conclusions

In this chapter, we searched for evidence of substructure within the GC systems of M86 and M84. We did so by creating surface density maps from the spatial distribution of GC candidates within the field and noting several features. We also split the GC population into red (metal-rich) and blue (metal-poor) subsamples to identify any new features and to what extent features discovered are dominated by red or blue GC candidates. Further, we collated kinematic data from two surveys of GCs in the field to understand the kinematics of identified features.

The surface density maps of the entire sample of GC candidates showed three interesting features. The first was a surface density peak offset from the center of M86 by $0.7'$. The dwarf galaxy, NGC 4406B, coincides with this surface density peak. Though we do not know how many of the GCs in our sample belong to NGC 4406B, dwarf ellipticals with similar luminosities are capable of hosting enough GCs to, at least partially, account for this over-density. Further, there is evidence to suggest that NGC 4406B is interacting with M86 and so a perturbation within the M86 GC system is possible (Elmegreen et al. 2000). The second feature identified was a bridge of elevated surface density connecting the M86 and M84 GC systems. This feature cannot be entirely explained by projection effects from two overlapping GC systems and may be a result of interactions between the two GC systems. The third structure found was a flattened iso-density contour along the southeast edge of the M86 GC system. This structure resembles a similar one found by Mihos et al. (2017) within the the low surface brightness starlight around M86. Mihos et al. (2017) called their structure the "SE Shelf" and argued that it may be the result of a major accretion event in M86's past.

We divided our GC candidates into two subsamples corresponding to red (metal-rich) and blue (metal-poor) colors. We found that the blue GC candidates dominate

all structures that were apparent in the total GC candidate sample (the surface density peak that was offset from the center of the M86 GC system, the elevated surface density bridge connecting the M86 and M84 GC systems, and the flattened iso-density contour along the southeast of the M86 GC system). In contrast to this, the structures mentioned all decreased in strength when analyzing the surface density maps of the red GC candidate sample. The red GC candidates were more centrally concentrated with boxier iso-density contours than the blue sample.

We found several examples of GCs with radial velocities inconsistent with the velocity of the nearest giant elliptical galaxy. The majority of these GCs appeared to be located within the bridge connecting the M86 and M84 GC systems. It may be that the GCs within this bridge have been stripped from their host; however, they may also simply be part of the outer GC population of these two massive elliptical galaxies. In our analysis we found possible evidence for a stream of intracluster GCs whose velocities are consistent with that of M84. This stream appears to form along the east-west axis of M86 and to the south of the M86 GC system.

References

Albaretti, F.D., et al. 2017, ApJS, 233, 25

Armandroff, T.E. & Zinn, R. 1988, AJ, 96, 92

Ashman, K.M. & Zepf, S.E. 1992, ApJ, 384, 50

Astropy Collaboration, Robitaille, T. P., Tollerud, E. J., et al. 2013, A&A, 558, A33

Astropy Collaboration, Price-Whelan, A. M., Sipőcz, B. M., et al. 2018, AJ, 156, 123

Beers, T. C., Flynn, K., & Gebhardt, K. 1990, AJ, 100, 32

Bekki, K., & Yahagi, H. 2006, MNRAS, 372, 1019

Bekki, K., & Yahagi, H. 2009, Globular Clusters - Guides to Galaxies, 373

Belokurov, V., Zucker, D. B., Evans, N. W., et al. 2006, ApJ, 642, L137

Belokurov, V., Erkal, D., Evans, N. W., et al. 2018, MNRAS, 478, 611

Binggeli, B., Sandage, A., & Tammann, G. 1985, AJ, 90, 1681

Blakeslee, J. P. 1999, AJ, 118, 1506

Bonfini, P., Zezas, A., Birkinshaw, M., et al. 2012, MNRAS, 421, 2872

Brodie, J.P. & Strader, J. 2006, ARA&A, 44, 193

Cappellari, M., Emsellem, E., Krajnović, D., et al. 2011, MNRAS, 413, 813

Côté, P. 1999, AJ, 118, 406

Crnojevic, D., Sand, D.J., Spekkens, K., Caldwell, N., Guhathakurta, P., McLeod, B., Seth, A., Simon, J.D., Strader, J., & Toloba, E. 2016, ApJ, 823, 19

D'Abrusco, R., Fabbiano, G., Strader, J., et al. 2013, ApJ, 773, 87

D'Abrusco, R., Fabbiano, G., & Zezas, A., 2015, ApJ, 805, 26

D'Abrusco, R., Cantiello, M., Paolillo, M., et al. 2016, ApJ, 819, L31

de Vaucouleurs, G., de Vaucouleurs, A., Corwin Jr., H.G., Buta, R.J., Paturel, G., & Fouque, P. 1991, Third Reference Catalogue of Bright Galaxies (New York: Springer)

Deason, A. J., Belokurov, V., Koposov, S. E., et al. 2018, ApJ, 862, L1

Durrell, P. R., Côté, P., Peng, E. W., et al. 2014, ApJ, 794, 103

El-Badry, K., Quataert, E., Weisz, D. R., et al. 2019, MNRAS, 482, 4528

Elmegreen, D. M., Elmegreen, B. G., Chromey, F. R., & Fine, M. S. 2000, AJ, 120, 733

Ferguson, A. M. N., Irwin, M. J., Ibata, R. A., et al. 2002, AJ, 124, 1452

Ferguson, A. M. N., & Mackey, A. D. 2016, Tidal Streams in the Local Group and Beyond, 191

Forbes, D. A., & Bridges, T. 2010, MNRAS, 404, 1203

Forte, J.C., Martinez, R.E., & Muzzio, J.C. 1982, AJ, 87, 1465

Gaia Collaboration, Prusti, T., de Bruijne, J. H. J., et al. 2016, A&A, 595, A1

Hargis, J. R., & Rhode, K. L. 2012, AJ, 144, 164

Hargis, J. R., & Rhode, K. L. 2014, ApJ, 796, 62

Harris, W.E. & van den Bergh, S. 1981, AJ, 86, 1627

Helmi, A., Babusiaux, C., Koppelman, H. H., et al. 2018, Nature, 563, 85

Hopkins, P. F., Kereš, D., Oñorbe, J., et al. 2014, MNRAS, 445, 581

Hopkins, P. F., Wetzel, A., Kereš, D., et al. 2018, MNRAS, 480, 800

Ibata, R. A., Gilmore, G., & Irwin, M. J. 1994, Nature, 370, 194

Ibata, R., Irwin, M., Lewis, G., et al. 2001, Nature, 412, 49

Iodice, E., Spavone, M., Cantiello, M., et al. 2017, ApJ, 851, 75

Ivezić, Ž., Connolly, A., VanderPlas, J., Gray, A. 2014, Statistics, Data Mining, and Machine Learning in Astronomy, (Princeton University Press)

Janowiecki, S., Mihos, J. C., Harding, P., et al. 2010, ApJ, 715, 972

Ko, Y., Hwang, H. S., Lee, M. G., et al. 2017, ApJ, 835, 212

Lambert, R. A., Rhode, K. L., & Vesperini, E. 2020, ApJ, 900, 45.

Li, H., & Gnedin, O. Y. 2014, ApJ, 796, 10

Lim, S., Peng, E. W., Duc, P.-A., et al. 2017, ApJ, 835, 123

Longobardi, A., Arnaboldi, M., Gerhard, O., et al. 2015, A&A, 579, A135

Longobardi, A., Peng, E. W., Côté, P., et al. 2018, ApJ, 864, 36

Lu, N. Y., Hoffman, G. L., Groff, T., et al. 1993, ApJS, 88, 383

Mackey, A. D., Huxor, A. P., Ferguson, A. M. N., et al. 2010, ApJ, 717, L11

Madrid, J. P., O'Neill, C. R., Gagliano, A. T., et al. 2018, ApJ, 867, 144

Mieske, S., Infante, L., Benítez, N., et al. 2004, AJ, 128, 1529

Mihos, J. C., Harding, P., Feldmeier, J. J., et al. 2017, ApJ, 834, 16

Miller, B. W., & Lotz, J. M. 2007, ApJ, 670, 1074

Muzzio, J.C., Martinez, R.E., & Rabolli, M. 1984, ApJ, 285, 7

Myeong, G. C., Evans, N. W., Belokurov, V., et al. 2018, ApJ, 863, L28

Park, H. S., Lee, M. G., & Hwang, H. S. 2012, ApJ, 757, 184

Peng, E. W., Jordán, A., Côté, P., et al. 2006, ApJ, 639, 95

Powalka, M., Puzia, T. H., Lançon, A., et al. 2018, ApJ, 856, 84

Ramos, F., Coenda, V., Muriel, H., et al. 2015, ApJ, 806, 242

Ramos-Almendares, F., Abadi, M., Muriel, H., et al. 2018, ApJ, 853, 91

Ramos-Almendares, F., Sales, L. V., Abadi, M. G., et al. 2020, MNRAS, 493, 5357.

Rhode, K. L. 2012, AJ, 144, 154

Rhode, K.L. & Zepf, S.E. 2001, AJ, 121, 210

Rhode, K.L. & Zepf, S.E. 2003, AJ, 126, 2307

Rhode, K.L. & Zepf, S.E. 2004, AJ, 127, 302

Rhode, K.L., Zepf, S.E., Kundu, A., & Larner, A.N. 2007, 134, 1403

Robert, M.S. & Haynes, M.P. 1994, ARA&A, 32, 115

Romanowsky, A. J., Strader, J., Brodie, J. P., et al. 2012, ApJ, 748, 29

Rudick, C. S., Mihos, J. C., & McBride, C. K. 2011, ApJ, 732, 48

Schaye, J., Crain, R. A., Bower, R. G., et al. 2015, MNRAS, 446, 521

Strauss, M. A., Huchra, J. P., Davis, M., et al. 1992, ApJS, 83, 29

Silverman, B., 1986, Density Estimation for Statistics and Data Analysis, (Chapman and Hall)

Springel, V., White, S. D. M., Jenkins, A., et al. 2005, Nature, 435, 629

Springel, V., Wang, J., Vogelsberger, M., et al. 2008, MNRAS, 391, 1685

Tonry, J.L., Blakeslee, J.P., Ajhar, E.A., Fletcher, A.B., Luppino, G.A., Metzger, M.R., & Moore, C.B. 2001, ApJ, 546, 681

Tully, R.B. 1988, Nearby Galaxies Catalog (Cambridge: Cambridge University Press)

Tully, R.B., Courtois, H.M., Dolphin, A.E., Fisher, J.R., Heraudeau, P., Jacobs, B.A., Karachentsev, I.D., Makarov, D., Makarova, L., Mitronova, S., Rizzi, L., Shaya, E.J., Sorce, J.G., & Wu, P.-F. 2013, AJ, 146, 86

van Zee, L., Barton, E.J., & Skillman, E.D. 2004, AJ, 128, 2797

Vogelsberger, M., Genel, S., Springel, V., et al. 2014, MNRAS, 444, 1518

Yahagi, H., & Bekki, K. 2005, MNRAS, 364, L86

Young, M.D., 2016, ProQuest Dissertations Publishing

Zepf, S.E., & Ashman, K.M. 1993, MNRAS, 264, 611

Zinn, R. 1985, ApJ, 293, 424

Chapter 5

Conclusions and Future Work

5.1 Summary of Results

In the context of a ΛCDM Universe, hierachical formation suggests that galaxies evolve through the continual accretion of smaller proto-galaxies. In this paradigm the remnants of these processes should in many cases be observable as streams or shells of stellar material within the galaxies or regions surrounding them. Identification of such features can lead to valuable insight on the histories of these stellar systems that elucidate the role that various factors, such as environment and internal structure of the stellar system, play in galactic evolution. This dissertation probed the RGB stellar population of three Andromeda dwarf satellites and the GC systems of the M86 and M84 galaxies with the purpose of identifying such substructure and the possible effects of galaxy interactions.

5.1.1 Substructure Within the Dwarf Galaxies Lacerta I, Cassiopeia III, and Perseus I

In Chapter 3, we searched for substructure within the RGB population of the Lacerta I, Cassiopeia III, and Perseus I dwarf galaxies. Discovered within the last decade (Martin et al. 2013a,b) these three dwarf galaxies are satellites of the Andromeda galaxy. Due to their proximity to the Andromeda galaxy, these dwarfs may show evidence of tidal interaction within the distribution of their RGB stellar population.

I calculated the structural parameters of an exponential and general Sersic function that best fitted our data. With these structural parameters, a model was constructed to estimate the surface density at each point in a grid across our field. The estimated surface density at each of these points was then compared to the measured surface density. Using this method, deviations from the estimate suggest a perturbation in the RGB stellar distribution that is unaccounted for in our model and thus a candidate for substructure.

Applying this method to our observations of Lacerta I revealed a chain of over-densities, $2.5 - 3\sigma$ above the expected surface density, along the west side. The over-densities are connected by several lower-significance regions of elevated surface density and so may be a single coherent substructure spanning most of the length of the galaxy. Beyond two half-light radii, a low-significance filament appears to stretch at least partially in the direction of M31 but no other structures are visible.

Cassiopeia III has two over-densities that stretch from the center towards the southeast and northwest. The crowding within the central $3'$ of the image means that it is impossible to determine if these two over-densities are isolated or a single coherent substructure.

The RGB stellar population of Perseus I shows little evidence of substructure within two half-light radii or in the surrounding field. This lack of substructure may be a result of its relative isolation within its environment. Located $\sim$ 370 kpc east of M31, Perseus I is the most isolated of the three dwarf satellites in our sample and may simply not have had the tidal interactions necessary to form substructure within the spatial distribution of its stellar population.

5.1.2 Substructure Within the Globular Cluster Systems of M86 and M84

Chapter 4 described results from a search for substructure within the globular cluster (GC) populations of M86 and M84 using the spatial positions of 2250 GC candidates selected from wide-field, multi-color broadband imaging. We estimated the amount of contamination in the GC candidate sample and then applied statistical corrections to account for it. We then used the Kernel Density Estimation (KDE) technique to create surface density maps of the GC systems within the M86/M84 field and of the red and blue GC candidate subpopulations separately. We combined our KDE analysis results with kinematic data drawn from Park et al. (2012) and Ko et al. (2017) and analyzed the spatial positions and radial velocities of a subset of the GCs to see if a kinematic fingerprint could be identified.

We identified three main substructures within the field. First, we found the surface density peak of the M86 GC system was offset from the system's center by approximately $0.7'$. This over-density coincides with the dwarf elliptical galaxy, NGC 4406B. Although we unable to determine how many of the GCs in our sample are hosted by NGC 4406B, dwarf elliptical galaxies with similar luminosities can host enough GCs to account, at least partially, for this over-density. Moreover, Elmegreen et al. (2000) has found evidence for an interaction between M86 and NGC 4406B, so a perturbation within the M86 GC system caused by NGC 4406B is within the realm of possibility. The second structure detected was a bridge connecting the M86 and M84 GC systems, perhaps as a result of interactions between the two galaxies. The final structure was a flattened iso-density contour along the southeast edge of the M86 GC system. Mihos et al. (2017) found a similar structure in the low surface brightness starlight around M86 and argued that it may be the result of a major accretion event in the galaxy's past.

When we divided our GC candidates into red (metal-rich) and blue (metal-poor) subpopulations we found that the blue GC candidates were the dominant population in the structures mentioned above: the various features that were apparent when we examined the total GC candidate sample were also apparent when we observed the blue GC candidate subsample. In contrast, these features had a marked decrease in strength when analyzing the surface density map of the red GC candidate sample.

We found several examples of GCs with radial velocities that were inconsistent with the velocity of the nearest giant elliptical galaxy. The majority of such GCs were located within the bridge connecting the M86 and M84 GC systems. It is possible that the GCs within this bridge have been stripped from their host galaxy, but they may instead simply be part of the outer GC population of these two massive elliptical galaxies. Our analysis also showed possible evidence for a stream of intracluster GCs with velocities consistent with that of M84 emerging along the east-west axis of M86 and to the south of the M86 GC system.

5.2 Future Work

There are a two main avenues for further work based on the findings presented here. The first is obtaining spectroscopy of the stars or GCs located within the substructures detected in this work. Both Cassiopeia III and Lacerta I show possible substructure within their RGB stellar populations. Martin et al. (2014) have already performed spectroscopy on the stellar populations of Lacerta I, Cassiopeia III, and Perseus I. They used the spectroscopic data to confirm the galaxies are bound to M31, estimate the dynamical mass encompassed within the half-light radius of each galaxy, and determine the average metallicity of each galaxy. However, they did not analyze their sample for substructure within the velocity space. Future efforts could build on this dissertation by analyzing the other properties, such as kinematics and metallicity, of the stars within these galaxies to identify other possible fingerprints of substructure.

Likewise, more studies of the M86 and M84 GC systems could be done with the aim of measuring velocities and metallicities across a wider field of view. Measurements of velocities and metallicities of GCs both within and outside the substructures identified in this work could reveal kinematic and/or chemical signatures that would shed further light on the origin and history of the galaxies in the field. Since GCs are faint, and the objects are distributed over a wide area on the sky, doing such studies with large telescopes and/or wide-field imaging capabilities would be useful.

The second avenue for future work is to apply the methods detailed within this dissertation to a larger sample of galaxies than was studied here. A study of a large sample of galaxies with a range of masses, environments, and morphologies would enable an exploration of how substructures vary with these galaxy properties, possibly lending key insights into formation scenarios. The Vera C. Rubin Observatory will produce a high cadence, wide-field survey capable of producing deep images of galaxies beyond 20 Mpc which is ideal for this type of work. The survey will cover a broad range of wavelengths (0.3 to 1.1υm) across six filters (u, g, r, i, z, y) which will be ideal for observing stellar populations and GCs. The Vera C. Rubin Observatory white paper by Laine et al. (2018) is a relevant example of the type of project that can be done to advance our knowledge in this field. They propose pairing observations from the Wide-Fast-Deep survey with WFIRST/Euclid data to search for tidal stellar streams in integrated light. This combination of deep photometry and spectroscopy will have similar benefits when applied to tracers of substructure like those used in this dissertation (RGB stars and globular clusters). Their focus would be on Milky Way analogs with distances greater than 20 Mpc, a sample of several thousand galaxies, and cosmological simulations suggest that they could find new tidal stellar streams in 80-90% of their sample. These findings could then be compared to cosmological simulations to help constrain future simulations.

References

Elmegreen, D. M., Elmegreen, B. G., Chromey, F. R., & Fine, M. S. 2000, AJ, 120, 733

Foreman-Mackey, D., Hogg, D. W., Lang, D., et al. 2013, PASP, 125, 306.

Higgs, C. R., McConnachie, A. W., Irwin, M., et al. 2016, MNRAS, 458, 1678.

Ko, Y., Hwang, H. S., Lee, M. G., et al. 2017, ApJ, 835, 212

Laine, S., Martinez-Delgado, D., Trujillo, I., et al. 2018, arXiv:1812.04897

Martin, N. F., Slater, C. T., Schlafly, E. F., et al. 2013, ApJ, 772, 15.

Martin, N. F., Schlafly, E. F., Slater, C. T., et al. 2013, ApJ, 779, L10.

Martin, N. F., Chambers, K. C., Collins, M. L. M., et al. 2014, ApJ, 793, L14.

Mihos, J. C., Harding, P., Feldmeier, J. J., et al. 2017, ApJ, 834, 16

Park, H. S., Lee, M. G., & Hwang, H. S. 2012, ApJ, 757, 184

Ryan Lambert

Education

Indiana University Bloomington, IN
Ph.D. in Astronomy (Minor in Physics) December 2021

- Thesis: Searching for Substructure in the Stellar Populations of Dwarf and Giant Galaxies (Advisors: Katherine Rhode and Enrico Vesperini)

Appalachian State University Boone, NC
B.S. in Physics with a concentration in Astronomy (Minor in Mathematics) 2015

- Thesis: The Use of Ca I and Hγ in Determining Stellar Activity (Advisors: Richard Gray and Dale Wheeler)
- Distinctions: Graduated with Honors

Research Experience

Ph.D. Dissertation Research: Searching for Substructure in the Stellar Populations of Dwarf and Giant Galaxies 2015 –2021
Advisors: Katherine Rhode and Enrico Vesperini

- Analyzing the spatial distributions of astronomical sources (globular cluster candidates around the elliptical galaxies M84 and M86, and Red Giant Branch stars in M31 dwarf satellite galaxies) to search for evidence of major mergers or accretion events. Writing Python scripts to estimate the surface density of objects using kernel density estimation, estimating structural parameters of galaxies through maximum likelihood estimation, and calculating residual differences between expected surface density values and measured values. The M86/M84 data were obtained with the Mayall 4-m telescope and Mosaic camera. Data for the M31 satellite galaxies were taken with the WIYN 3.5-m telescope and pODI camera.

Undergraduate Research: The Young Stellar Analogs Project 2011 –2015
Advisor: Richard Gray

- Performed spectroscopy and photometry of 31 young, Sun-like stars. Reduced and analyzed data from the Dark Sky Observatory 0.8m to understand the sample's star-spot cycles and make inferences about Earth's space environment during the early history of the Solar System.

Undergraduate Thesis: The Use of Ca I and Hγ in Determining Stellar Activity 2014 –2015
Advisors: Richard Gray and Dale Wheeler

- As an offshoot of the Young Solar Analogs Project, I used our collection of spectra for the 31 solar analogs to probe the correlation of the Ca I and Hγ spectral lines to stellar activity.

Skills and Training

- **Programming languages and environments:** Python, Unix, C, IRAF, R
- **Software:** Github, LaTeX, Overleaf, Microsoft Office, Adobe Photoshop
- **Participant: Summer School in Statistics for Astronomers XIV** May 2018

Participated in a weeklong workshop on statistical techniques and software for astronomical research. Topics covered include: Bootstrap resampling, Bayesian inference, spatial statistics, and model selection. The workshop included tutorials within the R environment.

- **Dark Sky Observatory 0.8m Telescope (Appalachian State University)** 2013 –2015
  - Observed 4-6 nights a semester during the academic year, and 10 nights each summer. Collected data for undergraduate research and thesis.
- **Kirkwood 12-inch Refracting Telescope (Indiana University)** 2015 –Present
  - Used to observe stars, planets and the moon, during Kirkwood Observatory Open House nights. Taught the operation of the telescope for undergraduate majors course (A305: Modern Observational Techniques).

Teaching Experience

Instructor of Record *The Solar System (A100)* Summer 2019
Indiana University

- A 30-student online course designed for non-majors. Duties included designing the online course lectures, assignments, and final project as well as grading the material and holding regular office hours for students.

Instructor of Record *The Art of Astronomy (A107)* Summer 2018
Indiana University

- A 60-student online course designed to teach the basics of astrophotography to non-majors. Duties included designing and implementing the entirety of the online course and holding regular office hours for students.

Instructor of Record *Stars and Galaxies (A105)* Summer 2017
Indiana University

- A 30-student introductory course for non-majors and majors. Duties included 1 hour and 15 minute daily lectures and the creation, administration, and grading of all course content, such as quizzes, homework assignments, midterms, final exams, classroom demonstrations, and lecture material.

Associate Instructor *Modern Observational Techniques (A305)* Fall 2015, 2017, 2019
Indiana University

- A 30-student, high-level astronomy course for majors. The course was designed to teach proper technique for observing with large telescopes and reducing data with IRAF software. Responsibilities included grading exams and homework, teaching labs, and acting as a tutor for students.

Associate Instructor *Various Courses (A100, A107, A105)* 2016 –2019
Indiana University

- Assisted with various introductory astronomy courses for non-majors. Duties included grading assignments, holding office hours, running help sessions, administering exams, and attending all class meetings.

Astronomy Outreach Experience

- **Astronomy Outreach Coordinator for the IU Astronomy Department** Fall 2020, Spring 2021
  Manager for department outreach events. Responsibilities include acting as a point of contact for the public, maintaining the department twitter page, and coordinating event volunteers.
- **Volunteer for Wonderlab: After Dark** July 2019
  An annual event held at the Wonderlab Science Museum designed to engage adults. I operated one of the department's 8 inch Celestron telescopes so the attendees could view Saturn and Mars.
- **Volunteer for Wonderlab Astronomy Day** April 2018
  An event for small children (0-8 years of age) held at the Wonderlab Science Museum. I set up and ran a crater making activity booth and assisted with the set up of a booth for viewing a galileoscope and handling meteorites.
- **Astronomy Club Graduate Student Liaison** 2018 –Present
  Provide a bridge between the undergraduate officers of the local Astronomy club and the Astronomy department. Duties include providing food, preparing the department telescopes for use, and managing club requests.
- **Volunteer for Indiana University Science Fest** 2015–Present
  Science Fest aims to engage children from the elementary to the high school level with fun, educational activities that relate to different fields of science. I ran different activities through out the day, such as making comets, thermal imaging demonstrations, and drawing scale models of the solar system.
- **Volunteer at Kirkwood Observatory Open House** 2015 –Present
  The Kirkwood Observatory is an on-campus observatory that is no longer in use for scientific research. Every week the observatory is opened to the public with graduate students operating the telescope and answering questions.

Honors and Awards

- Frank and Margaret Edmondson Prize for Teaching Spring 2018
- Winner of the Undergraduate Student Research Competition for Appalachian State Research Day 2013

Professional Affiliations

American Astronomical Society 2015 –Present

Publications

[1] R. A. Lambert, K. L. Rhode, and E. Vesperini, "Substructure in the Globular Cluster Populations of the Virgo Cluster Elliptical Galaxies M84 and M86", *The Astrophysical Journal*, vol. 900, no. 1, p. 45, Sep. 2020. arXiv: 2008.01737 [astro-ph.GA].

[2] R. O. Gray, J. M. Saken, C. J. Corbally, M. M. Briley, R. A. Lambert, V. A. Fuller, I. M. Newsome, M. F. Seeds, and Y. Kahvaz, "The Young Solar Analogs Project. I. Spectroscopic and Photometric Methods and Multi-year Timescale Spectroscopic Results", *The Astronomical Journal*, vol. 150, no. 6, p. 203, Dec. 2015. arXiv: 1511.00279 [astro-ph.SR].

Conference Presentations

AAS Kentucky Area Meeting (Lexington, KY) — May 2020
Substructure in the Globular Cluster Populations of the Virgo Cluster Elliptical Galaxies M84 and M86 — Poster

American Physical Society March Meeting (Denver, CO) — March 2014
The Young Solar Analogs Project — Poster

Quadrennial Physics Congress (Orlando, FL) — November 2012
The Evolution of the Superstar Technique — Poster